Journal of Wind Engineering & Industrial Aerodynamics 267 (2025) 106233

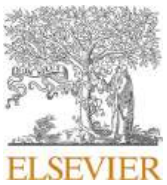

Contents lists available at ScienceDirect

Journal of Wind Engineering & Industrial Aerodynamics

journal homepage: www.elsevier.com/locate/jweia

A methodology for comparing mean, fluctuating and peak wind loads of buildings

Stefano Brusco [a], Timothy John Acosta [a,b], Yitian Guo [a], Jon Galsworthy [c], John Kilpatrick [d], Jin Wang [a], Gregory A. Kopp [a,*]

[a] Boundary Layer Wind Tunnel Laboratory, Faculty of Engineering, Western University, London, ON, N6A 5B9, Canada
[b] University of the Philippines Diliman, Quezon City, 1100, Philippines
[c] CPP Inc., 7365 Greendale Rd, Windsor, CO, 80550, USA
[d] RWDI, 600 Southgate Drive, Guelph, Ontario, Canada

ARTICLE INFO

Keywords:
Wind tunnel method
Building aerodynamics
Partial turbulence simulation
Vortex-shedding
Separating-reattaching flows
Measurement uncertainty

ABSTRACT

This paper proposes a methodology to distinguish true measurement uncertainty from aerodynamic effects when comparing load coefficients from different atmospheric boundary layer wind tunnels. It considers the similarity of the wind field through profiles of mean velocity, turbulence intensities, and gust factor, along with the distribution of fluctuating flow properties, especially at small scales of turbulence. To ensure consistency, peak wind velocities and responses are estimated from time-histories matched in full-scale sampling time, hence longer records are truncated to match shorter ones.

A test case involving a pressure model of a medium-rise building is proposed. It was independently tested by RWDI, CPP, and Western University under five different conditions. Time-histories of wind velocity and integrated aerodynamic base shear force, overturning, and torsional moments are analyzed and compared for nominally similar exposures. The trends in two comparisons are qualitatively consistent, with discrepancies in mean and peak coefficients not exceeding 7 % and 14 %, respectively. The analysis of the alongwind response reveals even smaller differences, especially in the mean coefficients, even across all five conditions.

These findings suggest that current wind tunnel testing standards could potentially be relaxed, particularly by incorporating Partial Turbulence Simulation concepts, without compromising the reliability of aerodynamic load predictions.

1. Introduction

Wind tunnel tests still represent the state-of-the-art methodology in wind engineering for the assessment of the aerodynamic loading on structures. Wind tunnel test standards and guidelines such as ASCE 49–21 (2021) provide guidance on properly designing wind tunnel tests according to the structure of interest. Comparing outcomes from studies conducted on the same test case from different facilities is an important task for post-disaster investigations, as well as for addressing questions about experimental uncertainties (e.g., Fritz et al., 2008; NIST, 2009; Zhu et al., 2025).

A notable example is represented by the World Trade Center, particularly Tower 2, which was examined following its tragic collapse in independent studies conducted by CPP Inc (2002) and RWDI (2002a, 2002b). Although the two investigations produced decidedly different predictions of the design wind loads on the structures, further evaluations ascribed such discrepancies to the combination of the wind tunnel test data with wind climate statistics rather than to actual differences in the aerodynamic data (Irwin, 2003; Vickery et al., 2003; Levy and Abboud, 2004).

For research purpose, a typical benchmark for tall buildings is the Commonwealth Advisory Aeronautical Research Council (CAARC) Standard Tall Building Model. This is a flat-roofed structure that is 184 m tall with a 3:2 rectangular cross-section (45.7 m × 30.5 m). A pioneering study was conducted by Melbourne (1980), who gathered data from five research centers carried out at different geometric scales (from 1:690 to 1:240 and for different levels of blockage) and examined the trends in the pressure and dynamic response measurements. The similarity of the reproduced wind fields was shown by comparing the vertical profiles of mean wind velocity, turbulence intensity (with values at

* Corresponding author.
E-mail address: gakopp@uwo.ca (G.A. Kopp).

https://doi.org/10.1016/j.jweia.2025.106233
Received 25 April 2025; Received in revised form 18 August 2025; Accepted 5 September 2025
Available online 13 September 2025

the top of the building between 8 % and 10 %) and the streamwise spectra at two thirds of the model height (i.e., close to the stagnation point). Several wind azimuths were investigated, spanning from 0° to 90°. Good agreement was observed between the datasets and Melbourne ascribed the scatter of the results to "*reasonable experimental accuracy*". Moreover, he noted that while pressure spectra on the windward face reflect the characteristics of the upstream terrain, the corresponding spectra in the leeward face appear to be much more similar. Melbourne concluded the paper stating that "*It might have been more interesting […] to have compared data measured in incorrectly modelled wind flows*", anticipating an interest in the effects of the upstream terrain on the results.

Melbourne's work inspired a line of research devoted to the study of the CAARC building. Tanaka and Lawen (1986) investigated the effects of the geometric scale of the model on the results, testing a 1:1000 model at the low-speed wind tunnel at the University of Ottawa. Obasaju (1992) conducted experiments at the British Maritime Technology (BMT) Environmental Wind Tunnel in a uniform wind profile and in a simulated atmospheric boundary layer (ABL) with a full-scale roughness height of 0.23 m, and turbulence intensity at the top of the building equal to 12.8 %. Different wind azimuths were tested. In particular, he observed how the effects associated with the transition from uniform profile to ABL depend on the wind azimuth. If the wind is normal to the wide face of the model, the drag coefficient increases in this transition, driven by a stronger base suction, with organized vortex-shedding persisting. Oppositely, for wind normal to the narrow face, the transition is accompanied by a weakening of the vortex-shedding with the drag coefficient and base suction being slightly lower, confirming a relationship that is typical of two-dimensional configurations (e.g., Roshko, 1993, for circular cylinders). Hence, an answer to Melbourne's original question is not straightforward, but it also depends on the aerodynamic situation at hand.

Still on the CAARC, an international benchmark study proposed by Holmes and Tse (2014) gathered and compared the results for the base moments estimated by means of high-frequency base balance tests by different facilities. A target profile for the mean wind velocity was provided, as well as target values of the longitudinal turbulence intensity and the integral length scale of turbulence at the rooftop. The coefficient of variation is in the order of 8–10 % when mean coefficients are compared, and the level of agreement is found to be better than Melbourne's results, "*perhaps reflecting less reliable experimental techniques at that time*", hence, introducing the role played by the measurement uncertainty associated with different digital acquisition systems and instrumentation errors in the comparison of results from different facilities. On the other hand, it grows up to 15–20 % when the peak dynamic response is studied, suggesting the sensitivity to the measurement of the spectra by the high-frequency base balance and the method of integration for considering the resonant component of the response.

Another noteworthy contribution to the use of high-frequency force balance techniques for comparing wind loads on tall buildings was presented by Chen et al. (2014). They compared data from the NatHaz Aerodynamic Loads Database (NALD) with results reported by other researchers (Cheng and Wang, 2004; Ha et al., 2004; Lin et al., 2005) for similar buildings tested in different test conditions, underscoring the value of such comparisons in supporting the preliminary design of tall buildings subjected to wind loads.

An important point to be considered to answer to Melbourne's comment concerns the different effects induced by the large and small scales of turbulence in the aerodynamic loading of structures. The pioneering research carried out by Bearman and Morel (1983) and Saathoff and Melbourne (1997) pointed out, on the one hand, the role played by the "rapid" small scales in affecting the flow characteristics around the body, and thus in determining the aerodynamic coefficients and, on the other hand, how the "slow" large scales affect the load in a quasi-steady manner. This has had significant implications for the testing of low-rise buildings, structures that are often replicated with a geometric scale that ranges between 1:10–1:100 to obtain adequate spatial resolution of pressures taps (Asghari-Mooneghi et al., 2016). At these geometric length scales, the reproduction of the target turbulence integral scale is prevented by the size of the experimental facility (Stathopoulos and Surry, 1983; Mokhtar et al., 2025), but this does not constitute a drawback for the studying of aerodynamic effects, as the effect may be re-established in the post-processing phase (Asghari-Mooneghi et al., 2016). This indicates that special attention should be given to an accurate simulation of the quicker, smaller fluctuations. This is the concept of "Partial Turbulence Simulation" (PTS), first conceived by Irwin (1998, 2008). Specific studies addressed on low-rise buildings (e.g., Asghari-Mooneghi et al., 2016; Akon and Kopp, 2016, 2018; Kopp et al., 2024; Guo et al., 2021; Estephan et al., 2022), have outlined the efficacy of this technique to replicate the aerodynamics governing the structure, in particular that relevant to the uplift (Kopp, 2023). Acosta et al. (2024a) pushed the limits of PTS further, proposing the definition of the terms E_S and E_L, representing the integrated area of the nondimensional spectra associated with the large and small scales respectively. Moreover, they suggested conditions of a maximum allowable deviation from the small-scale energy spectrum target, whose influence on mean, variances, and the statistical distributions are negligible. One outcome of this line of research is that it is possible to relax testing requirements and still obtain accurate predictions, at least for the uplift of low-rise structures. In contrast, one may wonder whether it is possible to translate this finding to slender structures. PTS is inherently applied to the design of slender structures, such as sectional models of bridge decks (e.g., Davenport and King, 1984; Irwin, 1998), enabling their studies by using turbulence grids deficient at low frequencies but adequately replicating the small-scale range of turbulence (Asghari-Mooneghi et al., 2016). The effectiveness of the methodology has been implicitly proven in the last years through the Benchmark on the Aerodynamics of a Rectangular 5:1 Cylinder, BARC (Bruno et al., 2014). In particular, Mannini et al. (2017) observed a shortening of the separation bubble on the lateral sides of their sectional model of elongated cylinders for increasing values of turbulence intensity. They also noticed that an increase of the energy content at the larger scale entails a longer separation bubble, with lower suction peak and higher values of pressure fluctuation, reflecting the behavior of the roofs of low-rise buildings (e.g., Akon and Kopp, 2016, 2018).

Summarizing, when examining the aerodynamic behaviour of a structure tested in different facilities, different results may be expected, even for nominally similar conditions. This is caused by measurement uncertainties and true aerodynamic effects. Moreover, the estimation of peak coefficients may also be affected by the considerable variability of the extreme value distributions (Gavanski et al., 2016).

Assuming that slight deviations in the simulated ABL lead to slight aerodynamic deviations, this paper proposes a methodology to correct them, and to limit the uncertainties in the definition of the peak coefficients, thus isolating the discrepancies associated with measurement uncertainties. These may be compared with those prescribed by the ASCE 49–21 (2021) limitations. A test case is examined, a medium-rise building that was independently tested by RWDI, CPP and Western University for different exposures, in the framework of the Consolidation of the ASCE 7–28 Main Wind Force Resisting Systems (MWFRS) Provisions (Guo et al., 2025; Kopp et al., 2025). It is a gabled-roofed building (6:12 slope) whose cross-section is rectangular (almost 3:1 ratio). Comparisons are firstly conducted for wind fields that are similar to each other. Hence, they are extended to take all the different exposures into account. Inspired by Obasaju (1992), two specific wind incidence angles (0° and 90°) are examined.

2. ASCE 49-21 standard requirements

To ensure compatibility between the wind tunnel scale and full-scale conditions, the most basic requirement is that the scale of model

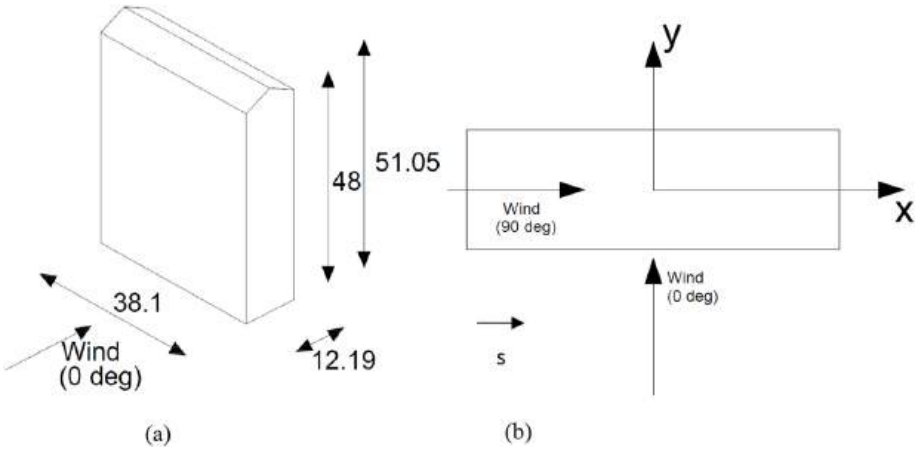

Fig. 1. (a) Geometry of the commonly tested wind tunnel model, (b) cross-section of the building and the Cartesian reference system. All the dimensions are in full-scale m.

matches the scale of the wind. This translates into three different prescriptions for the simulation of ABLs in ASCE 49–21 (2021):

$$\left(\frac{L_b}{z_o}\right)_m = \left(\frac{L_b}{z_o}\right)_p, \tag{1}$$

$$\left(\frac{L_b}{z_{ref}}\right)_m = \left(\frac{L_b}{z_{ref}}\right)_p, \tag{2}$$

$$\left(\frac{L_u}{L_b}\right)_m = \left(\frac{L_u}{L_b}\right)_p, \tag{3}$$

where L_b is the characteristic dimension of the building, z_o is the aerodynamic roughness length, z_{ref} is a reference height above ground where the wind velocity is referenced, L_u is the integral length scale of longitudinal (streamwise) component of the velocity; the subscripts m and p represent model scale and full-scale (prototype), respectively. Eq. (1), which represents Jensen number similarity, may be relaxed to be met within a factor of 3 to consider the uncertainties of full-scale quantities. By the same token, Eq. (3) has again to be met within a factor of 3, unless the modelled L_u is sufficiently higher than L_b:

$$\left(\frac{L_u}{L_b}\right)_m > 3. \tag{4}$$

Another requirement concerns the maximum blockage ratio of the model in the test section, which should be less than 5 %, albeit flexibility is allowed with adequate justification. Moreover, similarity of the Reynolds number, Re, is required, which is typically not possible to achieve. In ASCE 49–21, this requirement is relaxed to be:

$$Re = \left(\frac{L_b \overline{u}_b}{\nu}\right)_m \geq 11000, \tag{5}$$

where $\overline{u}_b$ is the characteristic velocity, and ν is the kinematic viscosity of the air.

Besides requirements on the simulation of the ABL, details concerning measurement techniques of rigid models (pertinent for the objectives of this paper) are required as well. The FS test duration, T_p, should be 500 times the integral time scale, I_t, which may be estimated as the ratio between L_u and $\overline{u}_b$. As far as the frequency resolution is concerned, the requirement is that reduced frequencies, $fL_b/\overline{u}_b$ (f being the frequency), up to 1 must be accurately resolved.

3. Wind tunnel test methodology

3.1. Geometry of the test case

The gable-roofed building configuration is characterized by the least and largest plan dimensions, w = 12.19 m and d = 38.10 m, respectively, and eave height, h_e = 48 m, while the mean roof height, h = 49.5 m, and the top roof height, h_T = 51 m. According to the categorization made by Wang and Kopp (2021), this structure is a medium-rise building. The geometry of the building is provided in Fig. 1a, while Fig. 1b illustrates the cross-section, defining the x- and y-axes; the z-axis is vertical and positive upward. Fig. 1b also provides the definition of the wind direction. The models were tested in an isolated configuration.

The tested wind tunnel models were manufactured by the three laboratories, each at a scale of 1:100. The numbers of pressure taps that were used to instrument the building are 632 for RWDI, 796 for CPP and 800 for Western. It is worth noting that the numbers of taps that were used to instrument the walls of the buildings are almost the same (121 on the walls parallel to the x-axis for RWDI and Western, 119 for CPP; 62 on the walls parallel to the y-axis for all the three laboratories). These taps may be grouped in eleven rings of pressure taps along the height that are in common between the different models. On the other hand, CPP and Western have higher density on the roof (434 taps) than RWDI model (266 taps). The numbers of tested exposures that were experimentally reproduced for each scale and for each type of measurement are 1 for RWDI and 2 for each of CPP and Western. This information is enclosed in Table 1 (the label UWO refers to Western), which also

Table 1
General overview of the 1:100 wind tunnel tests performed by RWDI, CPP and Western.

Label	Type of measurement	Number of tested exposures	Wind azimuths	Wind speed (at roof height), m/s	Sampling time, s	Sampling frequency, Hz	Re
RWDI	Pressure (632 pressure taps)	1	0°–90°, every 10°; 45°; 180°; 270°.	15.19	180	512	~ 336500
CPP	Pressure tests (796 pressure taps)	2	0°–350°, every 10°.	12.48/12.74	81.92	250	~ 276500/ 282200
UWO	Pressure tests (800 pressure taps)	2	0°–90°, every 10°.	8.71/9.52	180	625	~ 193000/ 210900

Fig. 2. Wind tunnel model and set-up tested by RWDI.

provides the tested wind orientations for each experimental campaign. In the following, only the wind orientation between 0° and 90°, with 10° step, will be considered for the analyses. Table 1 also encloses the estimation of the wind speed at the roof simulated during the tests, the sampling time and frequency, and the estimated Reynolds number, *Re* (Eq. (5)). It is noted that for a medium-rise building, all the geometric dimensions *h*, *w* and *d* play a role in defining the aerodynamics (Wang and Kopp, 2021); hence, L_b has been set as the average of the three quantities.

The next Sections will provide information about the different experimental facilities and the tested exposures. Each tested exposure derived from each dataset will be called Profile 1 and 2 (when available). In general terms, Profile 1 refers to an "Open" exposure, while Profile 2 refers to a "Suburban" one.

3.2. RWDI wind tunnel details

RWDI carried out the experimental campaign in their 3.70 m × 2.10 m boundary layer wind tunnel (BLWT). The configuration that was tested is referred to as RWDI – Profile 1. The turbulent properties of the wind were mainly reproduced through vertical spires installed at the inlet section of the facility. Profile measurements were conducted with a Cobra Probe that was installed at different heights. Acquisitions of the wind velocity time-histories in the three components, $u(t)$, $v(t)$, and $w(t)$ (i.e., longitudinal, lateral and vertical), were taken for a total of 60.16 s, sampled at 1200 Hz.

For wind load data, pressure measurements were acquired for 180 s, with a sampling frequency of 512 Hz. Details concerning the pressure measurement system and relevant correction are provided in Appendix A (for all participating institutions). During the tests, the reference wind velocity was taken from the reference Pitot-static tube in the wind tunnel, located 1.524 m (60") above the floor. However, the pressure coefficients are normalized to the velocity at $z = h_e = 48$ m full-scale (FS). The maximum blockage was 2.5 %. Fig. 2 shows a photograph of the set-up in the wind tunnel.

3.3. CPP wind tunnel details

The experimental campaign conducted by CPP was carried out in their BLWT, whose cross-section is 12 ft × 8 ft (3.66 m × 2.44 m), with a fetch of 55 ft (16.8 m). Two different exposures were simulated. They are referred to as CPP - Profile 1 and CPP – Profile 2. These are distinguished from each other because of different spires placed at the entrance of the wind tunnel and the height of roughness elements along the test section. In all cases, profile measurements were conducted with a hot-wire anemometer that was installed at various heights. Acquisitions of the longitudinal component of the wind velocity, $u(t)$, were conducted for 60 s, with a sampling rate of 2000 Hz.

For pressure measurements, the model was placed on the turntable with surrounding elements, as shown in Fig. 3. Data were acquired for 81.92 s, sampled at 250 Hz. The pressure coefficients are normalized by the reference wind velocity at 50.8 m FS. The maximum blockage is nominally 2 %.

Pictures taken in the facility are included in Fig. 3a and b, which show the set-up for the reproduction of Profiles 1 and 2, respectively.

3.4. Western wind tunnel details

The experimental campaign carried out by Western was conducted in the high-speed test section of the BLWT II. This wind tunnel offers a fetch of 39 m from inlet to the center of the turntable for flow development. The cross-section is 3.40 m in width and 2.40 m in height at the test location. For the simulation of both Profiles 1 and 2 (Fig. 4a–b), three 5-foot high spires were placed at the entrance of the wind tunnel. For Profile 2, a 1.25 ft (381 mm) barrier was placed across the wind tunnel section immediately downstream of the spires. Roughness elements of various heights for the two terrain conditions were used. Wind velocity measurements of $u(t)$, $v(t)$, and $w(t)$ were acquired for 181.76 s and sampled at 800 Hz using a Cobra Probe.

Pressure measurements were sampled at 625 Hz for 180 s. The pressure coefficients are normalized by the reference wind velocity at h = 49.5 m FS. The maximum blockage is lower than 2.5 %.

4. Wind field measurements

This Section presents the wind tunnel profiles from the three wind tunnels and discusses the similarities and differences between them, setting the stage for examination of the aerodynamic loads in Section 6.

4.1. Comparison A

Comparison A concerns Profile 1 exposures from RWDI and CPP. Profile 1 from Western is characterized by a profile of turbulence in-

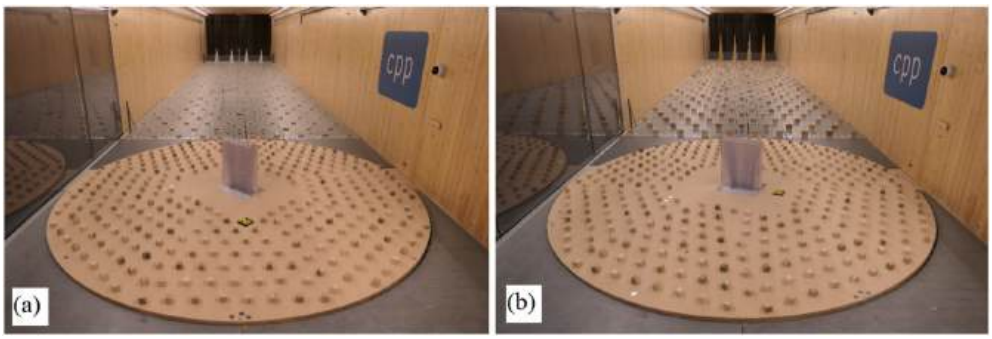

Fig. 3. Wind tunnel model and set-up tested by CPP for 1:100 scaled pressure model tests, (a) Profile 1 and (b) Profile 2.

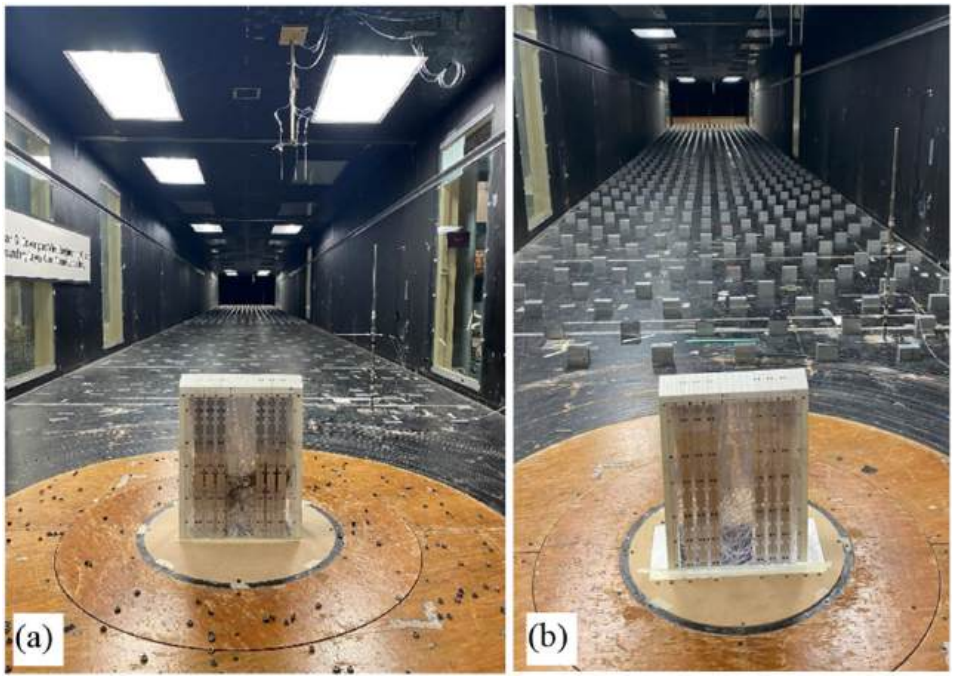

Fig. 4. Wind tunnel model and set-up tested by Western for 1:100 scaled pressure model tests, (a) Profile 1 and (b) Profile 2.

Table 2
Scaling of wind measurements for Comparison A (T_p = 2228 s).

Label	Velocity scale	Sampling time (s)
RWDI - Profile 1	2.70	60.16
CPP - Profile 1	2.45	54.59

tensity that is even lower in magnitude, hence it is not considered herein. The vertical profiles that are compared concern the non-dimensional mean wind velocity referenced to the reference height, $\overline{u}/\overline{u}_{z_{ref}}$ (where the horizontal bar indicates a temporal mean), the longitudinal turbulence intensity, I_u, and the integral length scales, L_u. The reference height, z_{ref}, is taken as the mean roof height, i.e., z_{ref} = h. The longitudinal turbulence intensity is defined as the standard deviation of the wind velocity in the longitudinal direction, σ_u, divided by $\overline{u}$, i.e., $I_u = \sigma_u/\overline{u}$. The integral length scales are determined by fitting the longitudinal wind velocity spectrum to the von Karman model (for further

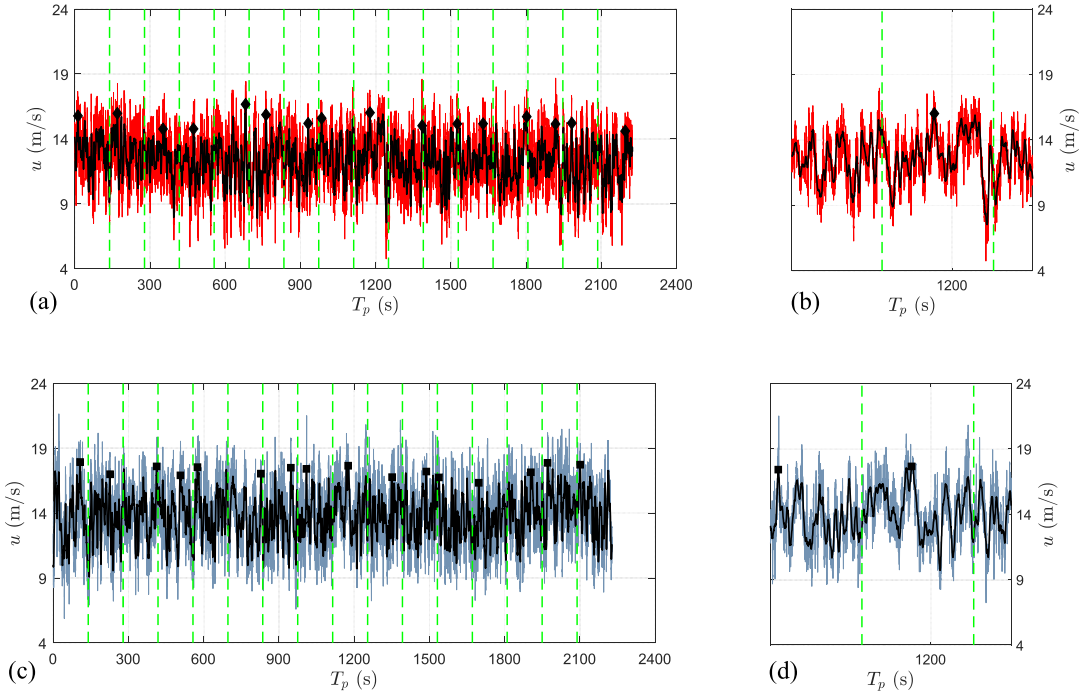

Fig. 5. Wind velocity time-histories in proximity of the stagnation height for Comparison A and definition of the 16 peaks on the 3-s FS filtered version (black signals) to perform the EVA: (a), (c) full time-histories and (b), (d) zoom on the 9th segment of RWDI – Profile 1 and CPP – Profile 1.

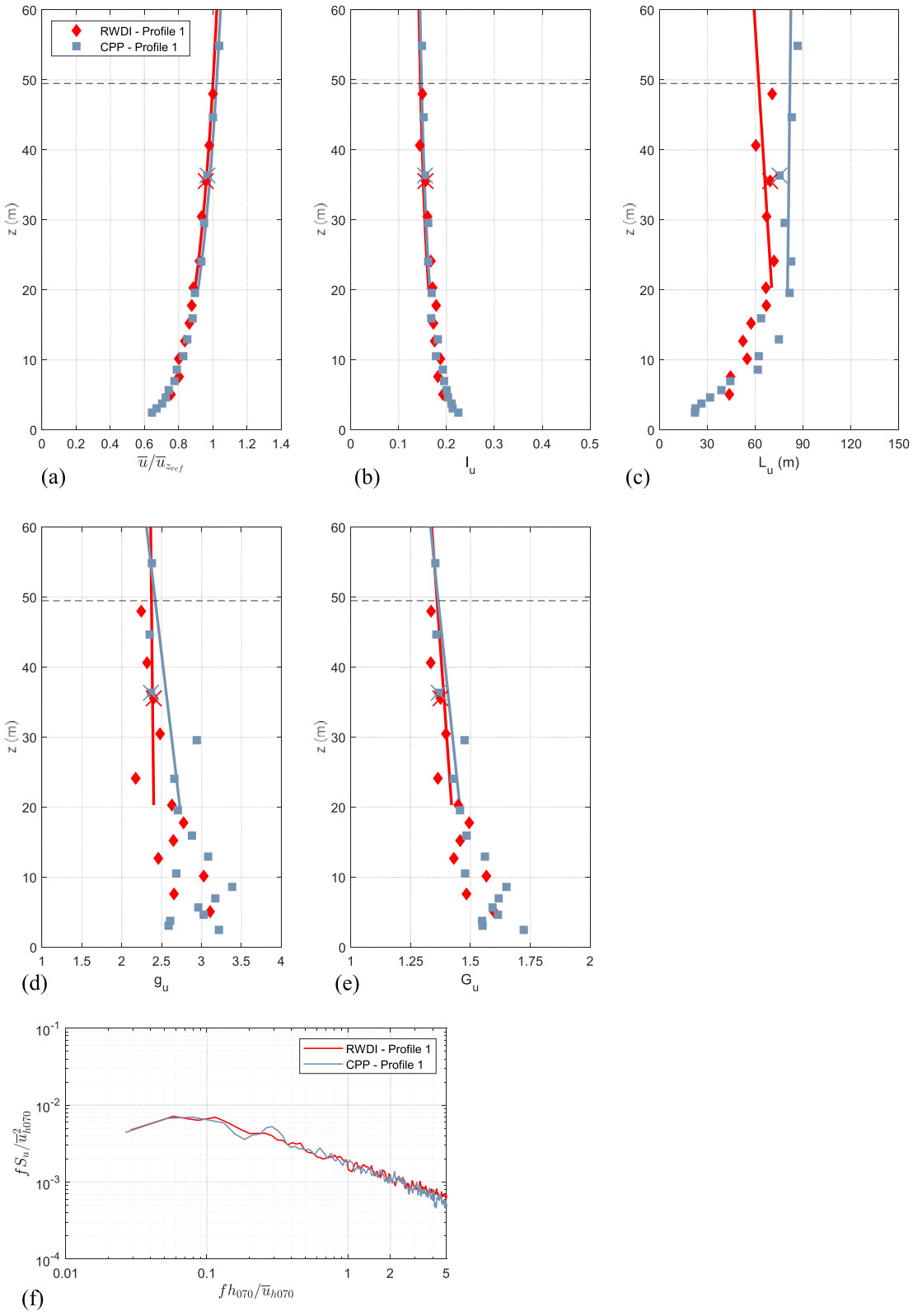

Fig. 6. FS equivalent vertical profiles and relevant fitting of (a) mean wind velocity, $\overline{u}/\overline{u}_{z_{ref}}$, (b) longitudinal turbulence intensity, I_u, (c) integral length scales, L_u, (d) peak factor, g_u, and (e) gust factor of the wind velocity, G_u, for Comparison A; (f) spectral comparison in correspondence of h_{070}. The legend in (a) applies to (b)–(e) as well, and the dashed line refers to h.

Table 3
Percentage differences of several wind field parameters estimated at h_{070} for Comparisons A (current Section) and B (Section 4.2).

Parameter	Percentage diff. (%), Comparison A	Percentage diff. (%), Comparison B
$\overline{u}_{h070}/\ \overline{u}_{z_{ref}}$	2.1	1.8
I_{uh070}	1.7	8.4
L_{uh070}	22.2	23.4
g_{uh070}	7.9	0.6
G_{uh070}	1.4	5.0

details, see Acosta et al., 2024b). The spectra are determined with the Welch's technique and adopting windows of 1 s (model scale) for all datasets. To evaluate the gust factor profiles of the wind velocity, it is necessary to perform an Extreme Value Analysis (EVA) on the acquired samples. To allow for a meaningful comparison, in particular to make the uncertainties typical of the EVA (e.g., Gavanski et al., 2016) uniform between the different datasets, the procedure proposed herein requires that the FS sampling times between the different datasets match. The velocity scale is based on the mean wind velocity estimated at z = 10 m FS. The time scale is evaluated as the ratio between the geometric length scale and the velocity scale, and hence the temporal length of the samples derived from the different laboratories are cut to match the same FS sampling time. Table 2 includes the velocity scales and the consequent temporal length to match 2228 s FS, which is the limit imposed, in this case, by RWDI's data. Consequently, CPP's acquisitions are cut to 54.59 s.

It is then possible to estimate the vertical profiles of the peak factor of the wind velocity, g_u. This, from each height considered for wind field measurements, is evaluated as:

$$g_u = \frac{\widehat{u} - \overline{u}}{\sigma_u}, \tag{6}$$

where $\widehat{u}$ is the peak 3-s FS wind velocity. This is evaluated, firstly, by filtering the signal with a 3-s moving average window, then cutting the time-history into 16 segments of 139.25 s. In each segment, the maximum 3-s wind velocity is obtained, and the 16 maxima are employed to estimate the relevant fitting parameters for the Gumbel distribution by adopting the Lieblein BLUE approach (Lieblein, 1974; Hong et al., 2013). Then, the Cook and Mayne method (Cook and Mayne, 1979; Gavanski et al., 2016) is employed to convert such parameters to a duration of 3600 s. Finally, the value with a probability of non-exceedance equal to 57 % is picked as $\widehat{u}$. Fig. 5a–c shows two wind velocity time-histories from RWDI – Profile 1 and CPP – Profile 1 (characterized by the same full-scale temporal length, 2228 s), in proximity of the stagnation height, $h_{070} \sim 0.70h$. The 16 segments are separated by the green dashed lines. In both cases, the black signals indicate the 3-s FS filtered signals, and the black dots display the maximum of each of the 16 segments. Fig. 5b–d depict closer views of the 9th segment.

Using this approach, the vertical profiles of the gust factor of the wind velocity, G_u, can be obtained, where:

$$G_u = \frac{\widehat{u}}{\overline{u}}. \tag{7}$$

The comparison between the vertical profiles as a function of the FS distance above the ground plane, z, for $\overline{u}/\overline{u}_{z_{ref}}$, I_u and L_u are presented in Fig. 6a, b and 6c, respectively. These graphs also include the relevant fitting along the height, for $z > 20$ m, as these curves embody the general trend throughout the considered height, contrary to single-point measurements. The height h is represented in the different profiles by the dashed horizontal line.

The first two plots indicate an excellent match between the two simulated wind fields, and both the profiles are characterized by a level of I_u close to 15 % at h. This is testified by the reduced percentages which summarize the corresponding differences estimated in correspondence of h_{070} through the different fitting (Table 3). On the other hand, the assessment of the integral length scales reveals slightly higher values for CPP's data. The comparison of the vertical profiles of g_u and G_u is documented in Fig. 6d–e, respectively. Qualitatively, it is possible to observe a higher level of scatter than is noticed in the previous quantities. Nonetheless, the level of agreement between the two datasets is still satisfactory, in particular for G_u (Table 3). Finally, Fig. 6f compares the estimated power spectral densities of the longitudinal component of turbulence at elevations close to the stagnation point on windward walls, $z = h_{070}$. These locations are highlighted in Fig. 6a–e with corresponding-colored crosses. The ordinate is $fS_u/\overline{u}^2_{h070}$, where S_u and $\overline{u}_{h070}$ are the power spectral density function and the mean wind velocity estimated at h_{070} respectively. The abscissa is instead the reduced frequency, $fh_{070}/\overline{u}_{h070}$. The comparison is again excellent, in particular at the smaller scales of turbulence. The corresponding comparison for the lateral component of turbulence is not possible, as not all the laboratories documented the relevant data using their standard methodologies.

Table 4
Scaling of wind field measurements for Comparison B (T_p = 1967 s).

Label	Velocity scale	Sampling time (s)
CPP - Profile 2	3.05	60.00
UWO - Profile 2	4	78.69

4.2. Comparison B

Comparison B uses the wind fields for Profile 2 produced by CPP and Western. As for Comparison A, the FS sampling times of the wind velocity acquisitions, T_p, are made coincident. In this case, this is equal to 1967 s, dictated by the 60 s of CPP's acquisitions. Thus, Western's data are cut to 78.69 s (Table 4).

Following the structure of Figs. 6 and 7 shows the FS vertical profiles and corresponding fitting (for $z > 20$ m) of $\overline{u}/\overline{u}_{z_{ref}}$, I_u, L_u, g_u and G_u (Fig. 7a–e). The height h_{070} is, once again, indicated with crosses in the profiles. The differences between the datasets estimated at h_{070} are included in Table 3, while the corresponding non-dimensional power spectral densities are shown in Fig. 7f.

The vertical profiles highlight apparent differences in the turbulent properties of the simulated wind field. For the turbulence intensity profile, the exposure reproduced by CPP is characterized by slightly higher levels, in particular close to the ground. On the other hand, the values of the integral length scales from the CPP's data appear to be slightly lower than those estimated from Western's data, especially for elevations above about 20 m FS. This is consistent with the spectral data displayed in Fig. 7f, which confirms the different distribution of energy in the two wind fields. It is noted that the two wind fields appear to be characterized by slightly more significant differences than those observed for Comparison A, particularly for I_u and G_u (Table 3). Nonetheless, the higher levels of flow turbulence than in Comparison A may still lead to comparable results, perhaps associated with a saturation of the effects induced by high-enough values of the flow energy at small scales (Akon and Kopp, 2018; Acosta et al., 2024a), which will be examined in Section 6.

5. Aerodynamic data

5.1. Definitions

For any tested wind direction, pressure coefficient time-histories, $C_{p,ref}$ (t), have been recorded. The subscript "ref" indicates that they are originally referenced through the reference wind velocity, $\overline{u}_{ref}$, taken at the reference height of the wind tunnel (i.e., outside the simulated ABL). For the generic i-th pressure tap, $C_{p,ref,i}$ (t) is:

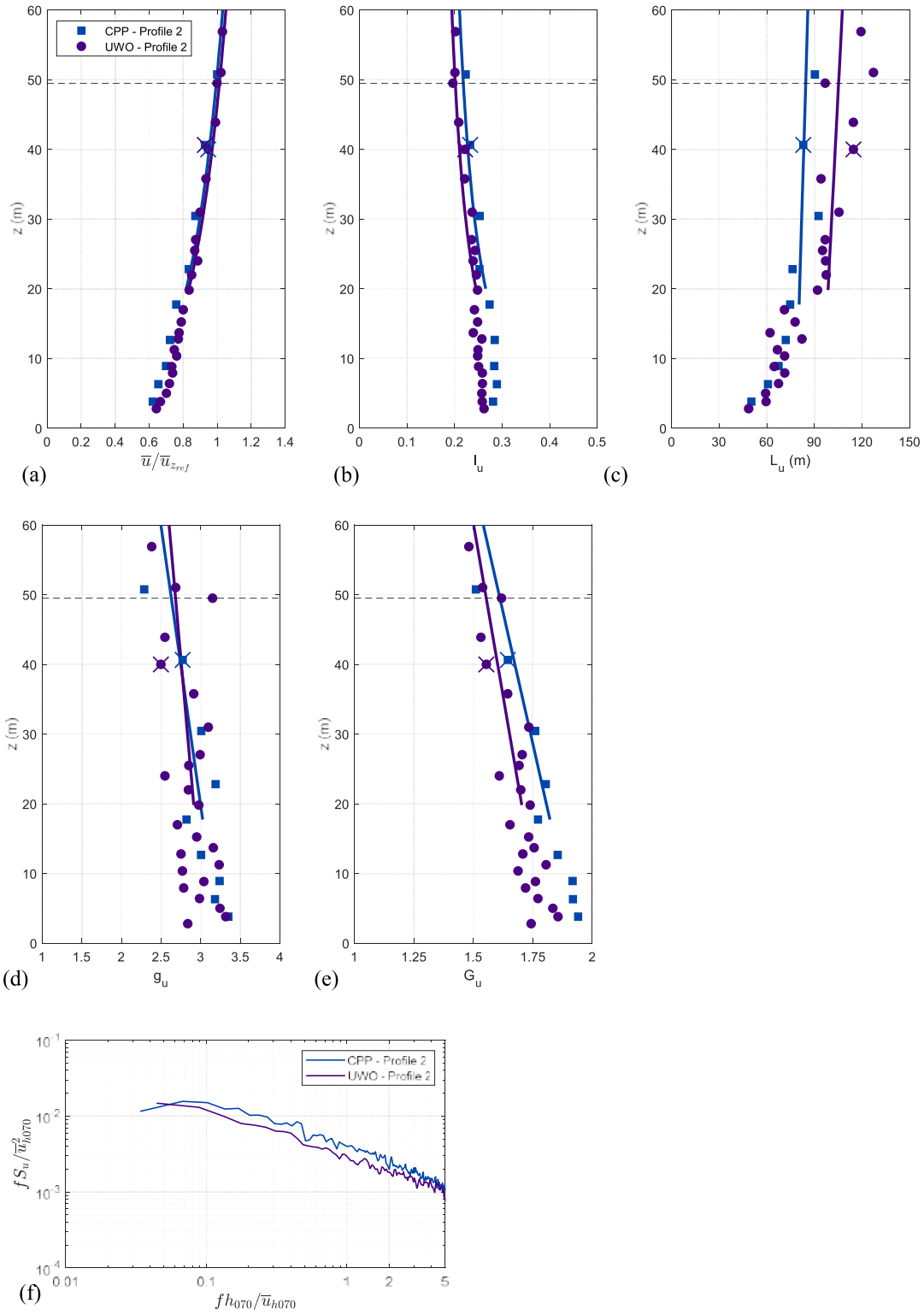

Fig. 7. FS equivalent vertical profiles and relevant fitting of (a) mean wind velocity, $\overline{u}/\overline{u}_{z_{ref}}$, (b) longitudinal turbulence intensity, I_u, (c) integral length scales, L_u, (d) peak factor, g_u, and (e) gust factor of the wind velocity, G_u, for Comparison B; (f) spectral comparison in correspondence of h_{070}. The legend in (a) applies to (b)–(e) as well, and the dashed line refers to h.

$$C_{p,ref,i}(\mathrm{t}) = \frac{p_i(t) - \overline{p}_s}{\frac{1}{2}\rho\overline{u}^2_{ref}}, \tag{8}$$

where $p_i(t)$ is the corresponding pressure time-history recorded by the pressure transducer, $\overline{p}_s$ is the mean value of the static pressure, and ρ is the air density. These coefficients are re-normalized to a reference height to the height of the roof, z_{ref}:

$$C_{p,z_{ref},i}(\mathrm{t}) = C_{p,ref,i}(\mathrm{t})\left(\frac{\overline{u}_{z_{ref}}}{\overline{u}_{ref}}\right)^2, \tag{9}$$

where $\left(\frac{\overline{u}_{z_{ref}}}{\overline{u}_{ref}}\right)$ is defined through the probe measurements conducted in absence of the building model. In the following, the dependence on time of the pressure coefficients will be implicitly considered, and the term (t) omitted.

Based on the integration of the whole set of $C_{p,z_{ref},i}$, it is possible to estimate the global aerodynamic coefficients, particularly, the base shear and overturning and torsional moment coefficients. The base shear force coefficients in the x- and y-directions, C_{F_x} and C_{F_y}, are defined as:

$$C_{F_x} = \frac{F_x}{\frac{1}{2}\rho \overline{u}^2_{z_{ref}} A_x}, \tag{10}$$

$$C_{F_y} = \frac{F_y}{\frac{1}{2}\rho \overline{u}^2_{z_{ref}} A_y}, \tag{11}$$

where F_x and F_y are the aerodynamic forces estimated in the x- and y-directions; A_x and A_y are the reference areas associated with the relevant direction (i.e., they are the frontal areas considering the wind direction, i.e., $A_x = wh$ and $A_y = dh_T$, where h_T is the total height of the building). Furthermore, C_{M_x} and C_{M_y} are the base overturning moment coefficients about the x- and y-axes, whereas C_{M_z} is the base torsional moment coefficient:

$$C_{M_x} = \frac{M_x}{\frac{1}{2}\rho \overline{u}^2_{z_{ref}} A_x h}, \tag{12}$$

$$C_{M_y} = \frac{M_y}{\frac{1}{2}\rho \overline{u}^2_{z_{ref}} A_y h_T}, \tag{13}$$

$$C_{M_z} = \frac{M_z}{\frac{1}{2}\rho \overline{u}^2_{z_{ref}} A_z h}, \tag{14}$$

where M_x and M_y are the base overturning moment generated by forces directed as the x- and y-axes (i.e., F_x generates M_x, whereas F_y generates M_y); M_z is the base torsional moment (about the z-axis), and A_z is the cross-section of the building, *wd*.

5.2. Measurement uncertainty

To properly compare aerodynamic results, and to confidently identify a change in pressure distributions following a change in aerodynamics, it is necessary to conduct a measurement uncertainty analysis. In fact, "*an estimate without a standard error is practically meaningless*" (Shelley et al., 2023). Appendix B illustrates the measurement uncertainty analysis that was conducted in detail, based on the thesis by Diaz (2006). The reader is also referred to Kwan and Kopp (2021). This procedure accounts for every factor of uncertainty associated with the experimental instrumentation at Western University (the same employed to conduct the experimental campaign of the test case object of this paper), encompassing the potential deviation of measured results from the actual "true" values. Outcomes of this procedure are the measurement uncertainties associated with the mean pressure coefficient $\overline{C}_{p,z_{ref}}$, $w_{\overline{C}_{p,z_{ref}}}$ (Eq. (B.7), and with the RMS pressure coefficient $\sigma_{Cp,z_{ref}}$, $w_{\sigma_{Cp,z_{ref}}}$ (Eq. (B.8). For sake of simplicity, the same uncertainties are used to estimate the deviations from the "true" values estimated through the experimental campaign conducted by RWDI and CPP.

6. Comparison of aerodynamic data

This Section describes the comparison of the pressure data, following the comparisons outlined in Section 4. As for the wind field measurement, the EVA of aerodynamic data to define the peak (maximum and minimum) coefficients, is performed by requiring that the time-histories from the different datasets are characterized by the same FS sampling time, T_p. Table 5 lists the FS sampling times that have been adopted for the datasets of Comparisons A and B. Specifically, for all the cases, T_p is dictated by the 81.92 s pressure acquisitions performed by CPP. RWDI's data have been cut to 68.51 s for Comparison A, while Western's data have been cut to 109.23 s for Comparison B because of differences in the velocity scales. The definition of the peak coefficient follows the procedure outlined for the peak wind velocities.

Table 5
Scaling of wind load measurements.

Label	FS sampling time, T_p (s)
Comparison A	2979
Comparison B	2731

It is noted that according to the requirements of ASCE 49–21 (Section 2), the duration of the test should be longer than 500 times the integral time scale of the wind tunnel. Considering the integral length scales simulated in the wind tunnels, and the corresponding wind velocity typical of the tests, this requirement is satisfied. Moreover, reduced frequencies $fL_b/\overline{u}_b$ up to 1 are accurately resolved, and the estimated Reynolds number typical of the experiments (Table 1) meet the requirements of Eq. (5).

The comparison is performed in terms of means, standard deviations, and peak values of the aerodynamic coefficients, with the peak coefficients referenced to the peak 3-s wind velocity using the gust factor, G_u, at $z = h$. All the global reaction time-histories are filtered with a moving-average window of 1 s FS, which mimics the effect of the mechanical admittance for a medium-rise buildings (Guo et al., 2025). Sections 6.1 and 6.2 are dedicated to Comparisons A and B.

6.1. Comparison A

The comparison between the aerodynamic data has been performed, firstly, through local analyses on single pressure taps and, secondly, considering global coefficients. A horizontal ring of pressure taps that is common to all the analyzed datasets is present at $z = 37.0$ m (h_{075}). This ring has 32 pressure taps (11 on the long sides and 5 on the short ones). For 0° wind incidence, Fig. 8a–c shows the distribution of the mean pressure coefficient, $\overline{C}_{p,h,}$ and the corresponding standard deviation, $\sigma_{Cp,h}$, as well as their standard errors, estimated through the measurement uncertainty analysis (Section 5.2). The subscript h indicates that these have been referenced to roof height. The abscissa "s/d" is a horizontal non-dimensional distance along the surface of the building that starts from one of the corners of the cross-section (Fig. 1b). If $s/d < 1$, the corresponding tap is located on the windward wall for 0°, while if $s/d > 1.3$ and $s/d < 2.3$ it is on the leeward wall; otherwise, it is located on one of the short lateral walls. The different sides of the building are separated through black dashed lines. The different curves exhibit similar values, suggesting a satisfactory agreement between the two datasets. The maximum difference estimated from the pressure coefficients reported in Fig. 8a is 0.07, while the minimum measurement uncertainty is estimated as 0.11 (Eq. (B.7). Fig. 8c leads to similar conclusions, with a maximum discrepancy equal to 0.03, whereas the minimum measurement uncertainty is 0.10 (Eq. (B.8). Hence, no apparent aerodynamic differences are found when comparing the datasets. The significant agreement is also confirmed when observing the trends along the height of the mean of the floor-by-floor alongwind shear force coefficients, $\overline{C}_{F_{y,z}}$ (Fig. 8b), and the corresponding standard deviation, $\sigma_{C_{Fy,z}}$ (Fig. 8d), estimated from the eleven horizontal rings of pressure taps.

Fig. 9a–c shows the time histories (filtered with 1-s FS moving average window, Guo et al., 2025) of the base shear force coefficients in the y-direction, C_{F_y}, again for the 0° wind incidence, along with the peak values in each segment. To determine the peak values, the 16 maxima and minima were extracted from the time-histories. Fig. 9b–d provide

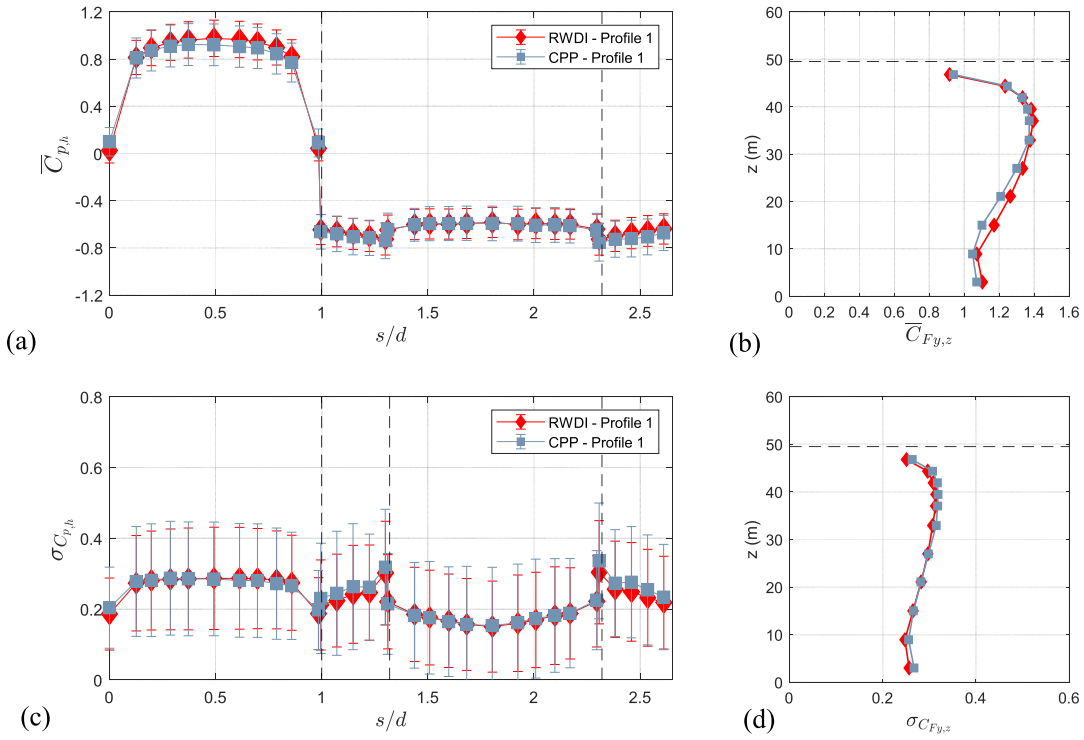

Fig. 8. Comparison for 0° of wind incidence: (a) mean and (c) standard deviation pressure distribution with their standard errors of the ring of pressure taps at 37.0 m (h_{075}) for Comparison A; variation with the height of the (b) mean and (d) standard deviation alongwind floor-by-floor coefficient.

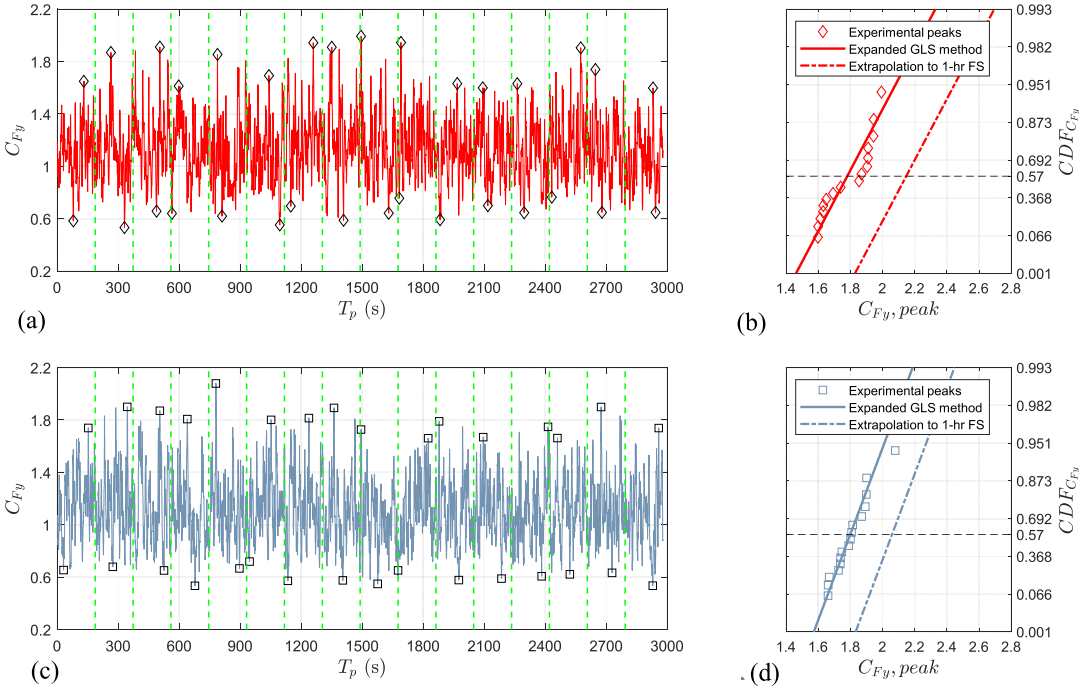

Fig. 9. (a), (c) 1-s FS filtered base shear force coefficient in the y-direction time-histories for Comparison A and definition of the 16 peaks for 0°, (b), (d) EVA and extrapolation to 1-hr FS; (a) and (b) are relevant to CPP data, whereas (b) and (d) are relevant to RWDI data.

the peaks and the fit using the Lieblein (1974) BLUE approach (Hong et al., 2013; Gavanski et al., 2016), along with the extrapolation to 1-hr FS through the equations proposed by Cook and Mayne (1979). The value with a probability of non-exceedance equal to 57 % of this distribution (horizontal black dashed line) corresponds to 2.15 for RWDI – Profile 1 and 2.06 for CPP – Profile 1.

Fig. 10 is structured as a 4 x 3 grid that includes the comparison between mean, standard deviations, peak values and peak values referenced to the peak wind velocity (1st, 2nd, 3rd and 4th row, respectively) of the base shear force coefficients in the x- and y-

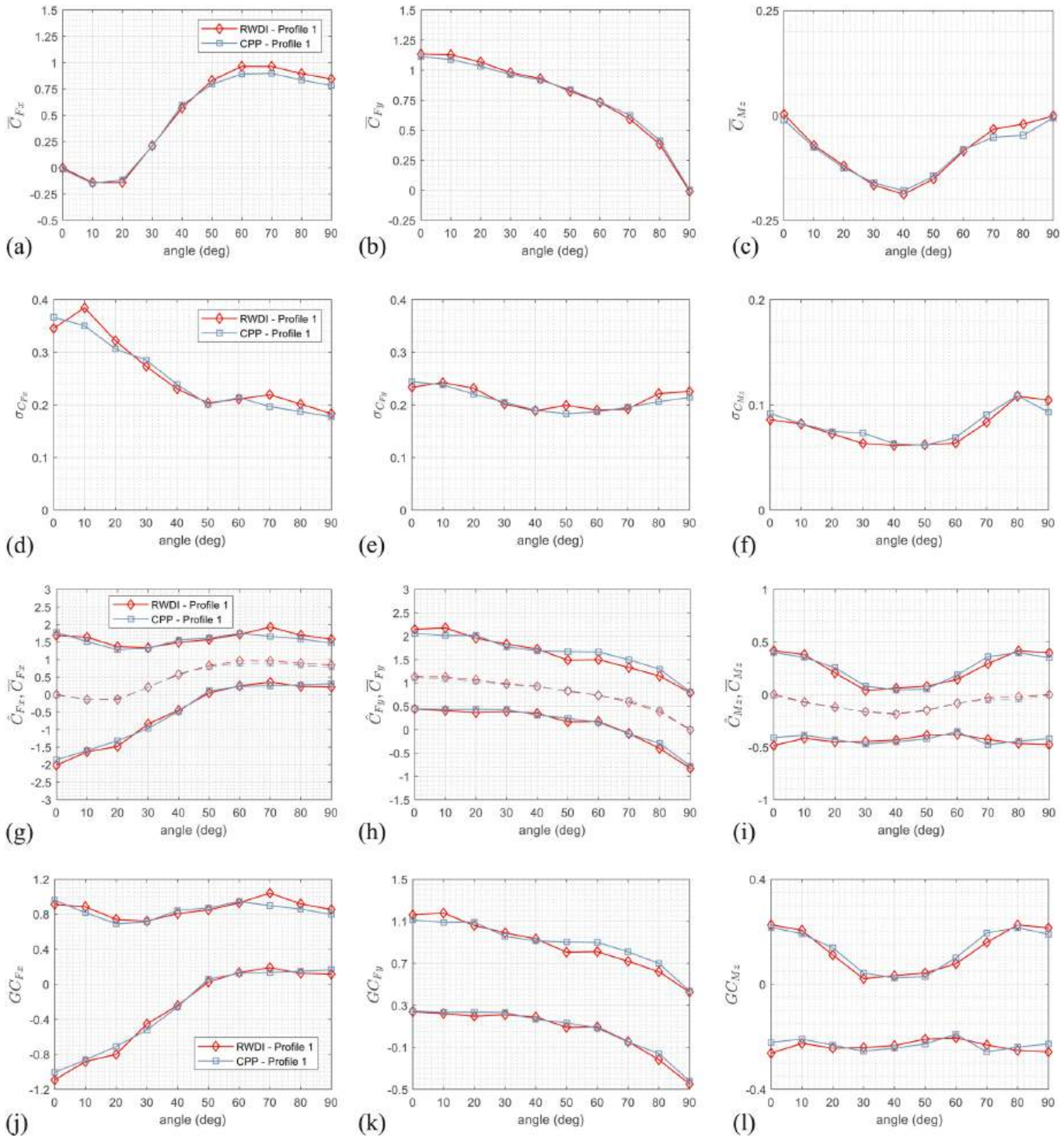

Fig. 10. Variation of statistical quantities of relevance for wind loading of the base shear force coefficients, C_{F_x} and C_{F_y} (1st and 2nd column), and torsional moment coefficient, C_{M_z} (3rd column): (a), (b), (c) mean values; (d), (e), (f) standard deviations; (g), (h), (i), peak coefficients; (j), (k), (l) peak coefficients re-referenced to the peak wind velocity at h. The legend in (a), (d), (g) and (h) applies to all.

direction, C_{F_x} and C_{F_y}, and the base torsional moment coefficient, C_{M_z} (1st, 2nd and 3rd column, respectively). For example, the mean value of C_{F_x}, $\overline{C}_{F_x}$, is shown in Fig. 10a, while its standard deviation, $\sigma_{C_{F_x}}$, is documented in Fig. 10d; the peak (maxima and minima) coefficients, $\widehat{C}_{F_x}$, are displayed in Fig. 10g, which also encloses the mean values $\overline{C}_{F_x}$ through dashed lines; the trend of the peak coefficients re-referenced to the peak wind velocity at h, GC_{F_x}, is shown in Fig. 10j. Plots concerning the base overturning moments are not reported for brevity, but are documented by Brusco et al. (2024). Each plot has the same abscissa, which expresses the wind azimuth.

Fig. 10 enables a qualitative comparison between the two datasets, which underlines a satisfactory agreement between the datasets over the range of tested wind directions, considering the similarity of the considered wind fields. The similarity appears to be highest for the principal directions (x, y) of the tested building (Fig. 1b), while for oblique winds the differences are slightly greater, already for the mean

Table 6
Summary of the maxima of the mean, fluctuating and peak (referenced to the peak wind velocity) values of base shear and base moment coefficients for Comparison A, with indication of the discrepancy.

Aerodynamic load	RWDI - Profile 1	CPP - Profile 1	Percentage diff. (%)
max ($\lvert\overline{C}_{F_x}\rvert$)	0.96 (60)	0.90 (70)	−6.9
max ($\lvert\overline{C}_{F_y}\rvert$)	1.13 (0)	1.11 (0)	−1.9
max ($\lvert\overline{C}_{M_x}\rvert$)	0.52 (60)	0.49 (70)	−6.0
max ($\lvert\overline{C}_{M_y}\rvert$)	0.54 (0)	0.54 (0)	−1.0
max ($\lvert\overline{C}_{M_z}\rvert$)	0.19 (40)	0.18 (40)	−4.4
max($\sigma_{C_{F_x}}$)	0.38 (10)	0.37 (80)	−4.7
max($\sigma_{C_{F_y}}$)	0.24 (10)	0.24 (0)	0.7
max($\sigma_{C_{M_x}}$)	0.19 (10)	0.18 (0)	−4.0
max($\sigma_{C_{M_y}}$)	0.12 (10)	0.12 (0)	2.4
max($\sigma_{C_{M_z}}$)	0.11 (80)	0.11 (80)	0.5
max ($\lvert GC_{F_x}\rvert$)	1.18 (10)	1.11 (0)	−5.4
max ($\lvert GC_{F_y}\rvert$)	1.09 (0)	1.01 (0)	−7.9
max ($\lvert GC_{M_x}\rvert$)	0.56 (70)	0.50 (70)	−11.9
max ($\lvert GC_{M_y}\rvert$)	0.57 (10)	0.54 (10)	−5.6
max ($\lvert GC_{M_z}\rvert$)	0.26 (0)	0.26 (70)	−1.7

coefficients (e.g., 60° for $\overline{C}_{F_x}$, or 70° for $\overline{C}_{M_z}$). It is noted that for these oblique wind azimuths, the coefficients are significantly affected by both the alongwind and crosswind responses. The similarity of the standard deviations of the coefficients is again satisfactory, and the most significant discrepancy is for 10° (for $\sigma_{C_{F_x}}$). The trends of the peak coefficients have similar variations.

Table 6 lists the maximum absolute values of the statistical quantities (one for each row) represented in Fig. 10 for the ten wind directions from each of the datasets. It is noted that the number between brackets defines the wind azimuth associated with the maximum coefficient. The last column provides a quantitative comparison of the differences.

As indicated by Table 6, the quantitative comparison of the maximum values of the coefficients is satisfactory. The maximum discrepancy concerning the mean values occurs for $\overline{C}_{F_x}$, which is 6.9 %, for wind incidences close to 60° −70°. The standard deviations exhibit an even closer agreement. Finally, also the peak responses associated with base shear force coefficients exhibit similar differences, with a maximum discrepancy equal to 7.9 % (for GC_{F_y} at 0°). Discrepancies for the base overturning moment are slightly higher, up to 11.9 % for GC_{M_x} at 70°. It seems worth considering that these discrepancies are lower than or similar to the uncertainties typical of the measurement of a single pressure tap (Fig. 8a–c). This may be associated with the overall similarity of the wind fields, which leads to global aerodynamic coefficients whose discrepancies are driven by the experimental instrumentation. In fact, this seems to be compelling with the requirements of ASCE 49–21, which states that the "*overall uncertainty in the reported results (aerodynamic coefficients) from instrumentation, sampling rate, and test duration shall be no greater than 10 %.*" (ASCE, 2021). Unsurprisingly, the maximum discrepancy is observed for peak values, which combine pressure/force measurements with wind velocity measurements. On the other hand, the choice of matching the FS sampling time is expected to have mitigated the discrepancies.

As a last piece of comparison, Fig. 11 shows the aerodynamic admittance, χ^2, for the alongwind base shear coefficient for 0° and 90° wind incidence (Fig. 11a–b). The definition of χ^2, for 0°, is provided as follows:

$$\chi^2(f) = \frac{\overline{u}_{h070}^2}{4\overline{C}_{F_y}^2} \frac{S_{C_{F_y}}(f)}{S_u(f)}, \tag{15}$$

where S_u and $\overline{u}_{h070}$ are the power spectral density function and the mean wind velocity at h_{070}, respectively, and $S_{C_{F_y}}$ is the power spectral density function of the alongwind base shear coefficient. The equation for 90° replaces C_{F_y} with C_{F_x}. The abscissa axes are reduced frequency, which is evaluated by considering the windward wall as the reference dimension. The aerodynamic admittances are well-aligned throughout the range of reduced frequency, close to the unitary line for the larger scales. Moreover, they also show the signature of the filtering procedure, and the agreement in their shape indicates the accuracy of the adopted velocity scales.

6.2. Comparison B

The description of the aerodynamic data concerning Comparison B (UWO – Profile 2 and CPP – Profile 2) is discussed here. Fig. 12 is structured as Fig. 10 and shows the trends of the different components of the load against the wind azimuth. Table 7 follows Tables 6 and it quantifies the maxima discrepancies between the datasets. Overall, Comparison B results in similar conclusions as Comparison A. Differences in the mean values are slightly better than Comparison A. In contrast, greater discrepancies are found for the fluctuating loads, which are more sensitive to differences in the properties of the flow turbulence. The maximum difference in the peak response is found for GC_{M_z} (13.7 %), while all the other discrepancies are lower than 10 %. This outcome seems consistent with the results of Comparison A.

7. Adjusting for the effects of the upstream terrain

7.1. Wind field profiles and spectra

In this Section, the results of the tests are adjusted to take the effects of the different upstream terrains into account. Fig. 13 provides the comparison between the different profiles of mean wind velocity (Fig. 13a), turbulence intensity (Fig. 13b), integral length scales of turbulence (Fig. 13c) and power spectral densities of these five simulations at the stagnation height, h_{070} (Fig. 13e). Additionally, Fig. 13d shows the fitted vertical profiles of the gust factor. All the figures include the data for RWDI – Profile 1, CPP – Profile 1, UWO – Profile 2 and CPP –

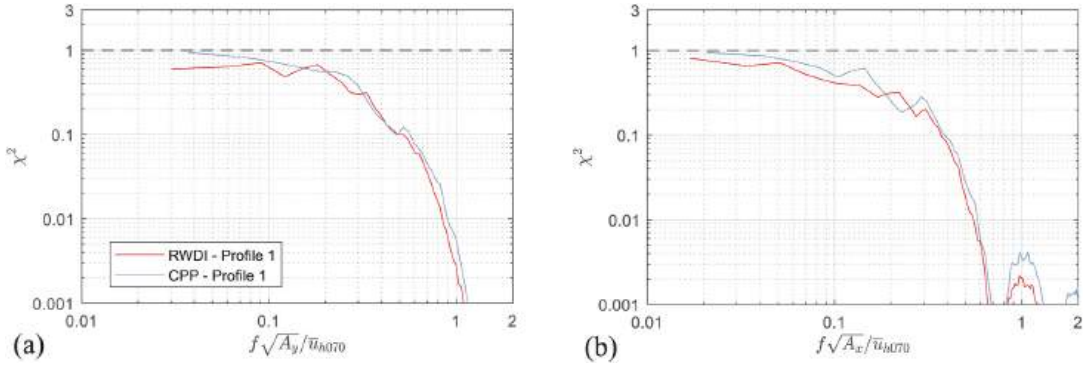

Fig. 11. Aerodynamic admittances of the alongwind base shear coefficient for Comparison A for (a) 0° and (b) 90 °.

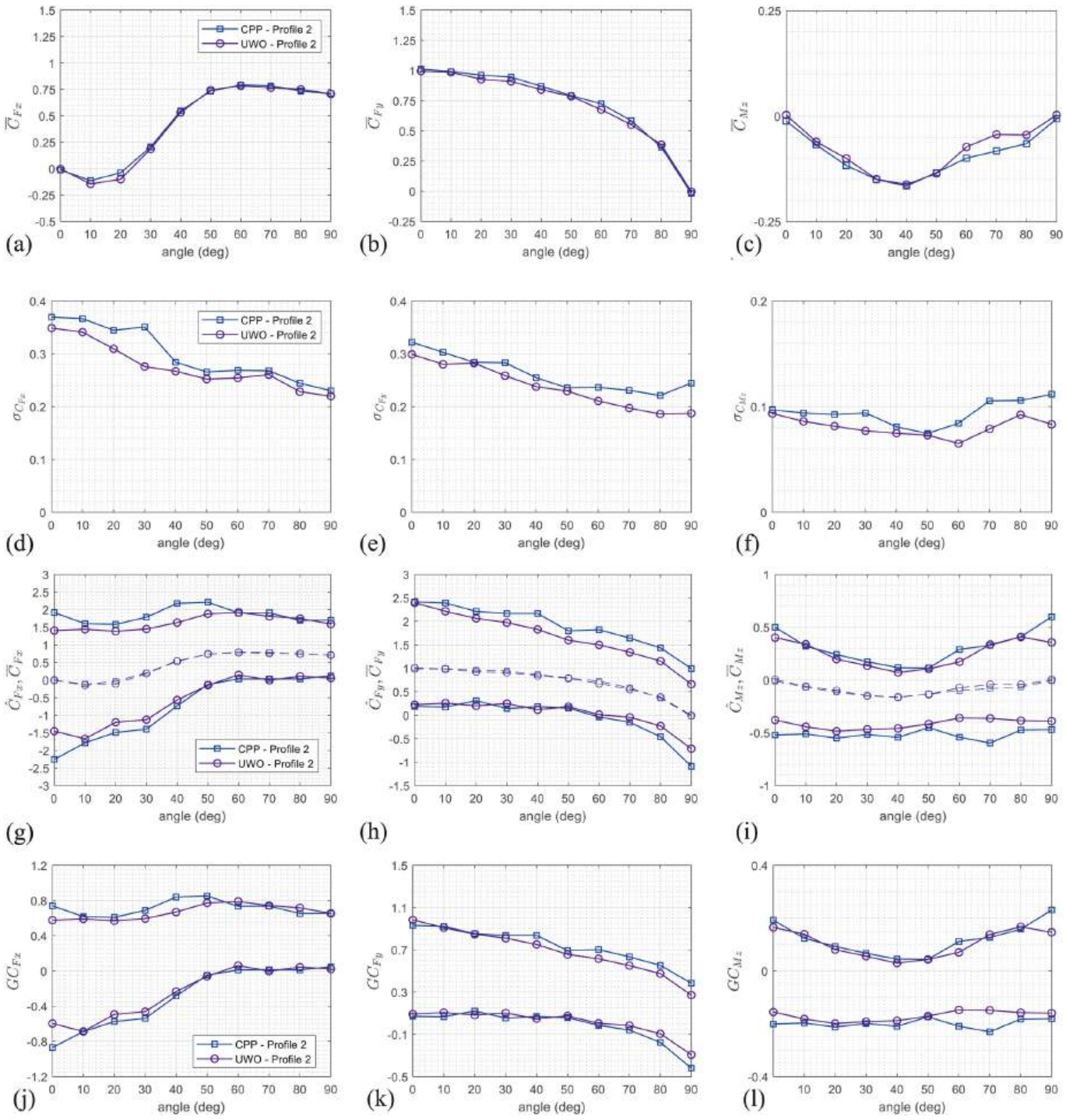

Fig. 12. Variation of statistical quantities of relevance for wind loading of the base shear force coefficients, C_{F_x} and C_{F_y} (1st and 2nd column), and torsional moment coefficient, C_{M_z} (3rd column): (a), (b), (c) mean values; (d), (e), (f) standard deviations; (g), (h), (i), peak coefficients; (j), (k), (l) peak coefficients re-referenced to the peak wind velocity at h. The legend in (a), (d), (g) and (h) applies to all.

Profile 2, as well as those from UWO – Profile 1. This latter exposure is the one characterized by the lowest G_u values. The number of samples that is adopted to analyze the relevant data are chosen to lead to a full-scale length of the wind velocity and aerodynamic loading time-histories that is consistent with the datasets for Comparison A. The differences in turbulence energy and integral scales are indicated by the differences in the spectra. Specifically, the spectra reflect an increase of the large scale of turbulence when considering UWO - Profile 1, RWDI – Profile 1, and CPP – Profile 1 (for $fh_{070}/\overline{u}_{h070} < 0.25$). Oppositely, the energy in the range of the small scales is similar in magnitude, overlapping when $fz/\overline{u}_{h070} > 0.25$. On the other hand, the mean wind velocity profiles appear more comparable, especially for $z > 25$ m.

The data from the different mean wind velocity and the gust factor (Fig. 13a–d) vertical profiles are used to estimate the coefficients that adjust the results to take the effects of the different upstream terrain into account (Sections 7.2 and 7.3).

7.2. *Pressure distributions at* $\boldsymbol{h_{075}}$

Before comparing the results from the different upstream terrains,

Table 7
Summary of the maxima of the mean, fluctuating and peak (referenced to the peak wind velocity) values of base shear force and base moment coefficients for Comparison B, with indication of the discrepancy.

Aerodynamic load	CPP - Profile 2	UWO - Profile 2	Percentage diff. (%)
max ($\lvert\overline{C}_{F_x}\rvert$)	0.79 (60)	0.78 (60)	−1.1
max ($\lvert\overline{C}_{F_y}\rvert$)	1.01 (0)	0.99 (0)	−1.8
max ($\lvert\overline{C}_{M_x}\rvert$)	0.44 (60)	0.44 (60)	−1.0
max ($\lvert\overline{C}_{M_y}\rvert$)	0.50 (0)	0.48 (0)	−3.0
max ($\lvert\overline{C}_{M_z}\rvert$)	0.17 (0)	0.16 (40)	−2.3
max($\sigma_{C_{F_x}}$)	0.37 (0)	0.35 (0)	−5.6
max($\sigma_{C_{F_y}}$)	0.32 (0)	0.30 (0)	−7.1
max($\sigma_{C_{M_x}}$)	0.19 (0)	0.17 (0)	−6.3
max($\sigma_{C_{M_y}}$)	0.16 (0)	0.14 (0)	−9.2
max($\sigma_{C_{M_z}}$)	0.11 (90)	0.09 (0)	−16.3
max ($\lvert GC_{F_x}\rvert$)	0.87 (0)	0.79 (60)	−9.2
max ($\lvert GC_{F_y}\rvert$)	0.93 (0)	0.98 (0)	5.6
max ($\lvert GC_{M_x}\rvert$)	0.42 (50)	0.41 (50)	−1.5
max ($\lvert GC_{M_y}\rvert$)	0.46 (0)	0.47 (0)	2.9
max ($\lvert GC_{M_z}\rvert$)	0.23 (90)	0.20 (20)	−13.7

the presence of different vorticity patterns governing the aerodynamics of the structure for different wind orientations is verified. This may be immediately proven by observing the mean pressure distribution of the common ring of pressure taps at the cross-section at $z = 37.0$ m (h_{075}) for different wind azimuths (0° and 90°). It is noted that the cross-section of the building is similar to a 1:3 rectangular shape. Assuming the wind to blow from the bottom of the plot to its top, Fig. 14a shows the mean pressure coefficient distribution extracted from CPP – Profile 2 for 0° (the cross-section is a plate characterized by a short afterbody), while Fig. 14b focuses on the distribution estimated for UWO – Profile 1 at 90° (the cross-section is an elongated rectangle). The former is characterized by mean pressure coefficients $\overline{C}_{p,h}$, on the lateral sides that are almost constant, and their magnitude is significantly negative. This is reflected on the pressure coefficients on the base (leeward wall), which are again negative. This is consistent with the effects of an alternate vortex-shedding affecting the structure, which is typical of two-dimensional configurations (e.g., Yu et al., 2013; Lunghi et al., 2024) and that persists in simulated boundary layers, as noted by Obasaju (1992). This seems to happen for all the exposures considered. The distribution of mean pressure coefficients at 90° is instead characterized by a significant variation of the coefficients on the lateral sides, which tend to zero in proximity of the trailing edge even for the exposure characterized by the lowest level of turbulence (i.e., UWO – Profile 1, Fig. 13b). This suggests the presence of a separating-reattaching flow, typical of elongated cylinders (e.g., Saathoff and Melbourne, 1997; Yu et al., 2013; Mannini et al., 2017) and roofs of low-rise buildings (Akon and Kopp, 2016, 2018; Morrison and Kopp, 2018).

The general trends observed in Fig. 14 are found for all the different datasets for the corresponding wind incidence, although effects associated with a different upstream exposure may be appreciated. Focusing on 0°, Fig. 15a–b shows the variation of the mean and the standard deviation of the pressure coefficients for all the five datasets. These coefficients have been re-normalized considering the height of the ring, h_{075} (Section 7.1; Liu et al., 2019). The abscissa follows a similar principle as in Fig. 8a–c, and it is equal to 0 at the corner where the flow separation occurs; however, it now encompasses only one of the lateral side and half of the leeward wall of the considered cross-section. Fig. 15a suggests an increase of suction when switching from Profile 1 to 2 exposures, with the values registered by CPP – Profile 2 that are too negative to be estimated from UWO – Profile 1 or RWDI – Profile 1, even considering the measurement uncertainties. The mean pressure coefficients derived from the Profile 1 triad decrease monotonically for the abscissa increasing towards the leeward edge, whereas the results from the Profile 2 cases exhibit a local increase at $s/d \sim 0.23$, perhaps suggesting an interaction between the vortices and the corner that is affected by the level of flow turbulence. The different curves become more similar in the leeward wall ($s/d > 0.31$), as in Melbourne's investigation, with the measurement uncertainties that encompass all the different results. The results associated with the standard deviation of the pressure coefficients (Fig. 15b) again reflect the different values of the turbulence intensity between the various datasets, in particular on the lateral wall. The magnitudes increase towards the edge with the leeward wall. Also in this case, it is possible to observe the shape gradually changing when moving from UWO – Profile 1 to CPP – Profile 2, exhibiting a relative maximum in correspondence of the mid-point of the lateral wall for higher level of turbulence intensity. The oscillations decrease on the leeward wall, but they still somehow reflect the different values of the incoming turbulence. In their whole, Fig. 15a–b point out a greater dispersion of the results on the lateral side rather than on the leeward side.

Analogously, Fig. 16 focuses on the results of 90°. The trend of the mean pressure coefficients on the lateral and leeward walls (Fig. 16a), estimated removing a static pressure offset (Kwan and Kopp, 2021), shows similar values of the maximum suction, with a change of its location, which becomes closer to the leading edge when moving from UWO – Profile 1 to the other exposures. The recovery of the pressures occurs for all the datasets, and it is reflected on similar values of the coefficients in the base. Also the trends of the standard deviation of the pressure coefficients let transpire the effects of different upstream terrains, with the maximum of the curves that significantly shifts in proximity to the leading edge for higher values of the turbulence intensity. This, accompanied by an increase of the magnitude, suggests the role played by the energy of the wind fluctuations, particularly those at the smaller scales. On the other hand, much less dispersion of the results is observed towards the trailing edge and in the leeward wall, in analogy with the outcomes of the BARC (Mannini et al., 2017; Lunghi et al., 2022; Mariotti et al., 2024). This outcome constitutes a formal analogy between the results observed at 0° and 90°, despite the different aerodynamic behaviour. This has implications on the comparison of the global aerodynamic loads in the alongwind direction, as deepened in the following.

7.3. Mean and peak aerodynamic base shear force in the alongwind direction

Table 8 lists the resulting values of the mean and peak responses of base shear coefficients in the alongwind direction, $\overline{C}_{F_d}$ and GC_{F_d} (i.e., $\overline{C}_{F_y}$ and GC_{F_y} for 0°, and $\overline{C}_{F_x}$ and GC_{F_x} for 90°) for the five datasets. The first number in each column is referenced to the roof height, h, while the second number is adjusted to take the corresponding profile shape of the mean/gust wind velocity into account, i.e., all the pressure coefficients have been re-normalized to the local height (Section 7.1). The last two rows indicate the coefficient of variation (c.o.v.), and the maxima difference in percentage between the values of the datasets. As can be seen, the correction reduces the differences, and all the c.o.v. are well below 10 %. The maxima percentage differences between the mean loads are estimated as 7.5 % and 8.9 % for 0° and 90°, which are higher than those estimated when comparing nominally similar terrain exposures (i.e., Comparison A, 0.4 % and 5.4 %, and Comparison B, 5.5 % and 4.3 %). Similar outcomes, but with higher discrepancies, are found for the peak responses, whose differences increase from 5.9 % to 8.9 % (Comparison A), and 6.3 % and 0.3 % (Comparison B), to 18.4 % and 23.9 %, with the coefficients that decrease when moving from Profile 1 to Profile 2 exposures. These differences may suggest the presence of an aerodynamic behavior that changes with the upstream terrain, confirming the comments made in Section 7.2. On the other hand, the results on the mean aerodynamic coefficients show a significant agreement, corroborating the limited dispersions of the pressure data in the leeward and windward walls that was visually appreciated (Section 7.2). This fact seems to substantiate the conclusions made by Acosta et al. (2024a) for the uplift

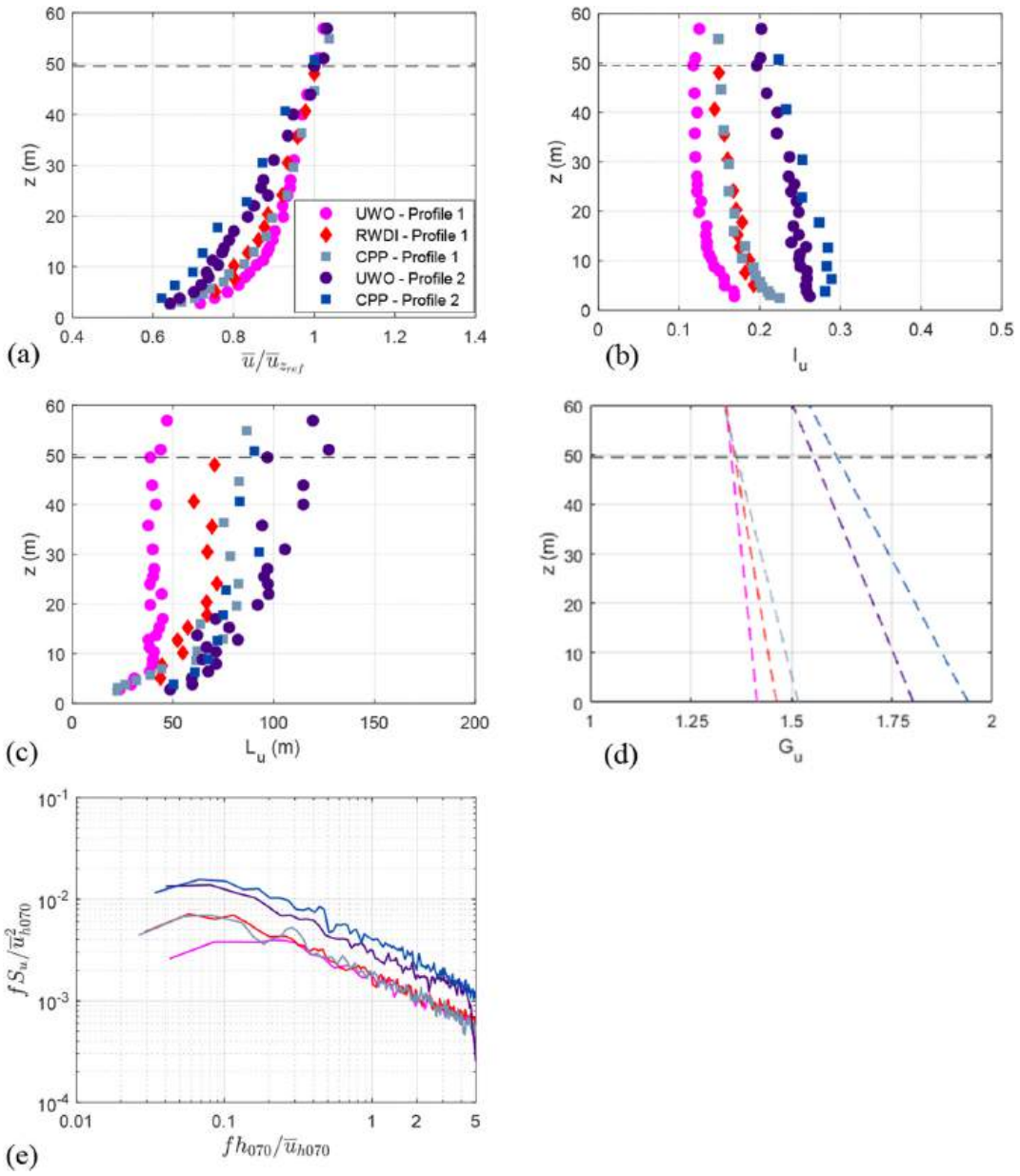

Fig. 13. Comparison between wind field measurements: vertical profiles (a) of mean wind velocity, (b) turbulence intensity, (c) integral length scale of turbulence, (d) fitted gust factor of the velocity for the five terrain simulations in the three boundary layer wind tunnels; (e) longitudinal wind velocity spectra at the nominal stagnation height (h_{070}). The legend in (a) applies to all.

of low-rise buildings, now generalized to the drag of a medium-rise structures characterized by aerodynamic phenomena typical of slender structures.

These remarks may be extended to take all the considered ten wind azimuths into account. Fig. 17a, b and 17c show the trends of the adjusted mean drag coefficients, their standard deviations and the peak responses. These once again confirm the considerations made before. The percentage difference that is estimated for the maximum value of the mean drag coefficient (observed for 50°/60° of incidence) is 6.9 %, while for the peak response is 18.7 %, again with the results from Profile 2 exposures being generally lower than those associated with Profile 1 exposures. These numbers reduce to 2.3 % and 0.9 % for Comparison A, and 3.4 % and 6.3 % for Comparison B, which appear even lower than those registered in Section 6. This is likely associated with the analysis being conducted on the alongwind direction only, hence mitigating the uncertainties induced by the crosswind response. The results of the standard deviations (Fig. 17b) reflect the different levels of turbulence intensities.

8. Conclusions

This paper proposes a methodology to separate true measurement uncertainty from aerodynamic effects caused by differences in the simulated wind fields, allowing the comparison of the aerodynamic data of buildings tested in different ABL wind tunnels. The methodology is based on assessing the similarity of the simulated wind fields and on the matching of the full-scale sampling time of the various time-histories of interest. The latter is crucial to limit, or at least to make uniform, the level of uncertainties that are associated with the EVA process of both wind velocity and aerodynamic data. The former one is necessary to estimate coefficients that allow the adjustment of the aerodynamic coefficient to the upstream terrain. If the considered exposures are nominally similar, the discrepancies should be limited and ascribable to measurement uncertainties (∼ 10 %). Conversely, if the wind fields are

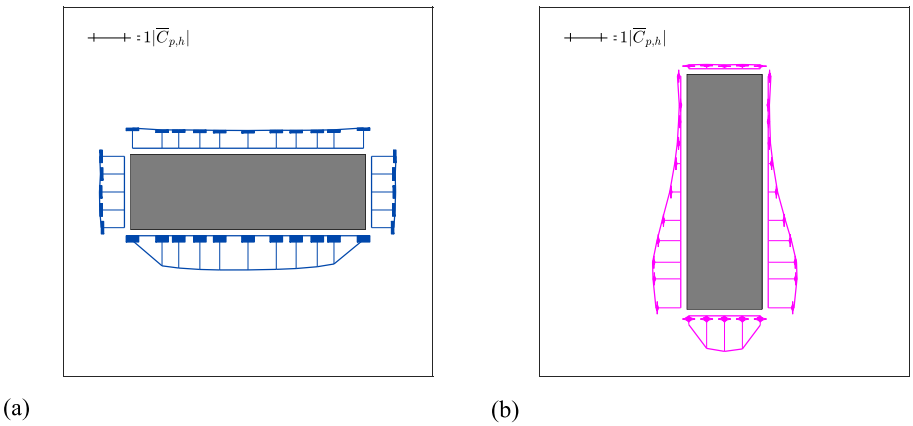

Fig. 14. Mean pressure distribution of the ring of pressure tap at $z = 37.0$ m for (a) 0°, CPP – Profile 2 and (b) 90°, UWO – Profile 1. The wind is directed from bottom to top.

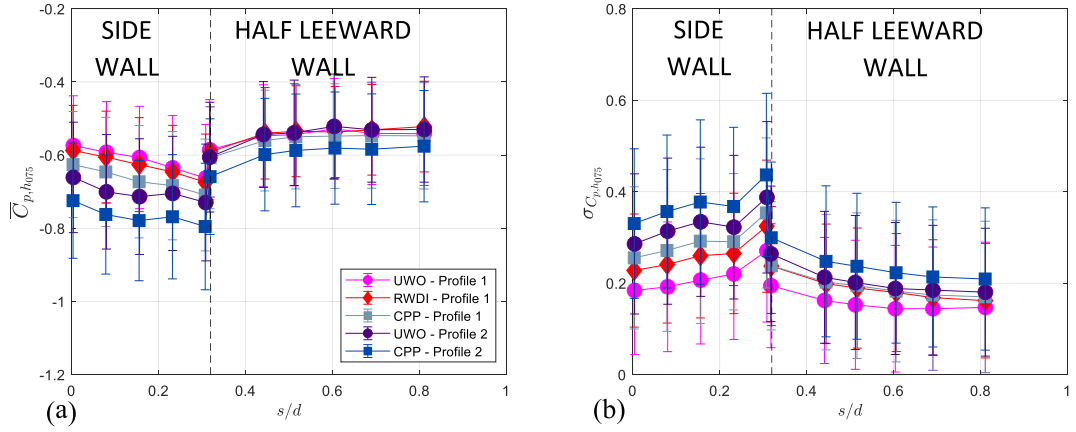

Fig. 15. Comparison of the distribution of the pressure coefficients in correspondence of the ring of pressure taps at $z = 37.0$ m for 0 ° of wind incidence: (a) mean and (b) standard deviation on the lateral side and half of the leeward side. The legend in (a) applies to (b) as well.

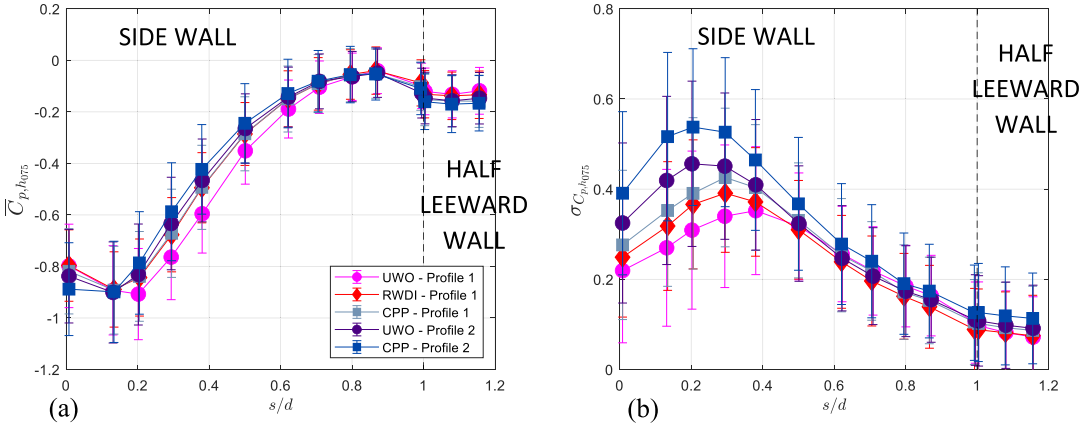

Fig. 16. Comparison of the distribution of the pressure coefficients in correspondence of the ring of pressure taps at $z = 37.0$ m for 90° of wind incidence: (a) mean and (b) standard deviation on the lateral side and half of the leeward side. The legend in (a) applies to (b) as well.

not nominally similar, the discrepancies between the adjusted coefficients may reflect true aerodynamic differences that arise because of the different upstream terrain.

A test case, a medium-rise rigid building independently tested from RWDI, CPP and Western University for different exposures of turbulent ABL (Open and Suburban), is proposed. The geometric scale is 1:100 for all the considered experiments, and a total of five different exposures were tested. When comparing results for nominally similar exposures, the results lead to satisfying agreements for the estimated aerodynamic loading. In particular, the discrepancies that are found when comparing the maxima of the mean aerodynamic coefficients are always lower than 7 %, while they reach 13.7 % when considering the peak response. Overall, these results comply with the requirements by ASCE 49–21, which prescribes an overall uncertainty of 10 % for instrumentation,

Table 8
Summary of the original and corrected mean and peak responses of base shear coefficients in the alongwind direction, $\overline{C}_{Fy}$ and $\overline{C}_{Fx}$, and GC_{F_y} and GC_{F_x}, at 0° and 90° of wind incidence for the five datasets.

	$\overline{C}_d$ $(\equiv \overline{C}_{F_y})$ (0 deg), original/ adjusted	$\overline{C}_d$ $(\equiv \overline{C}_{F_x})$ (90 deg), original/ adjusted	GC_d $(\equiv GC_{F_y})$ (0 deg), original/ adjusted	GC_d $(\equiv GC_{F_x})$ (90 deg), original/ adjusted
UWO – Profile 1	1.13/1.37	0.80/0.97	1.07/1.24	0.78/0.91
RWDI – Profile 1	1.13/1.41	0.84/1.05	1.16/1.35	0.85/0.99
CPP – Profile 1	1.11/1.42	0.78/1.00	1.10/1.28	0.79/0.91
UWO – Profile 2	0.99/1.40	0.71/0.99	0.99/1.21	0.66/0.81
CPP – Profile 2	1.01/1.48	0.71/1.04	0.93/1.14	0.65/0.80
C.o.v. (%)	5.6/2.4	6.9/3.1	7.8/5.6	10.6/8.2
Max. percentage diff. (%)	14.0/7.5	19.6/8.9	24.8/18.4	30.7/23.9

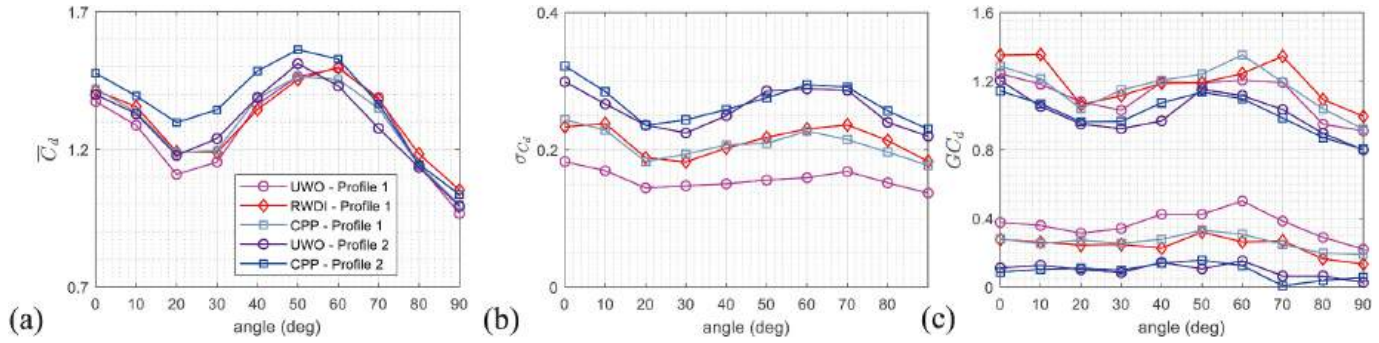

Fig. 17. Variation of the (a) adjusted mean, (b) standard deviation and (c) adjusted peak (re-referenced to the peak wind velocity) alongwind drag coefficient against the tested wind orientation for the five datasets. The legend in (a) applies to all.

sampling rate and test duration effects.

The presence of (at least) two aerodynamic mechanisms affecting the loads, in particular the crosswind response, are observed. Their presence is found to be consistent with the literature of two-dimensional rectangular prisms (Yu et al., 2013). When comparing all the five experiments for 0° and 90° wind azimuths, the effects of different levels of turbulence energy and scales are mainly reflected on the distributions of pressures on the lateral sides, while a greater agreement is found on the distributions governing the alongwind forces (windward and leeward walls). In fact, the resulting mean loads in the alongwind direction become comparable when adjusted to take the shapes of the mean wind velocity profiles into account, with discrepancies again lower than 10 %. The comparison of the corresponding peak responses suggests a reduction in the loads when moving from Open to Suburban exposures. When extending the comparison to the cases of oblique winds, an even more complex flow mechanism is likely to be observed, with shear layers separated from the leeward face and one of the lateral sides interacting with each other. Nonetheless, the discrepancy between the five maxima of the mean alongwind response is 6.9 %. They drop to even lower values for nominally similar exposures, confirming the reduction of the differences when considering the mean alongwind response only. This fact opens the doors to a generalization of the relaxation of requirements for wind tunnel testing in turbulent ABL flows proposed by Acosta et al. (2024a) for low-rise buildings to slender structures. Nonetheless, it seems noteworthy to recall that slender structures are characterized by an aerodynamic loading which also depends on the spatial uniformity of the incident wind fields, especially for structures whose wind loading is driven by an alternate vortex-shedding. Hence, specific and dedicated analyses should be conducted on unveiling this aspect.

CRediT authorship contribution statement

Stefano Brusco: Writing – original draft, Visualization, Validation, Software, Methodology, Investigation, Formal analysis, Data curation, Conceptualization. **Timothy John Acosta:** Validation, Methodology, Formal analysis, Conceptualization. **Yitian Guo:** Validation, Methodology, Formal analysis, Conceptualization. **Jon Galsworthy:** Supervision, Funding acquisition, Conceptualization. **John Kilpatrick:** Supervision, Funding acquisition, Conceptualization. **Jin Wang:** Supervision, Methodology, Conceptualization. **Gregory A. Kopp:** Supervision, Methodology, Funding acquisition, Formal analysis, Conceptualization.

Declaration of competing interest

The authors declare that they have no known competing financial interests or personal relationships that could have appeared to influence the work reported in this paper.

Acknowledgments

This work was funded by the Structural Engineering Institute of the ASCE. The Authors gratefully acknowledge the support of an Advisory Group made up of members of the ASCE 7 Wind Loads Sub-Committee, in particular Don Scott who chaired the Advisory Group, and Larry Griffis, Tim Reinhold, and Peter Vickery who provided significant guidance.

APPENDIX A. PRESSURE MEASUREMENT DETAILS

The pressure system used for the study conducted by RWDI was based on the Scanivalve ZOC33 minature pressure scanners and ERAD 4000 pressure measurement system. For pressure measurements, tubes measuring 48 inches (1219.2 mm) in length connected the pressure taps and the

pressure scanners. Correction of tubing resonance effects was performed using a digital correction technique based on the measured tubing transfer function (Irwin, 1979).

As concerns CPP's experimental campaign, all sensor miniature low pressure transducers were connected to a National Instruments Data Acquisition System. The tubing system consists of a 60 inches (1524.0 mm) long and 0.054 inches (1.4 mm) diameter tube with restrictors to give sufficient frequency response. All data is compensated for tubing distortion.

For pressure measurements carried out at Western, tubes measuring 30 inches (762.0 mm) in length connected the pressure taps and the solid-state high-speed pressure scanners. This system is made up of a 13-inch PVC tube, with an internal diameter of 0.053 inches (1.3 mm), connected to the model via a pass-through plate. Additionally, a 1.25-inch (31.75 mm) brass tubing extends into the sealed chamber, along with two restrictors. To connect to the pressure scanner, a 13-inch (330.2 mm) PVC tube with an internal diameter of 0.034 inches (0.9 mm) is used. The tubing system has a flat frequency response to about 200 Hz. Further details may be found in Ho et al. (2005).

APPENDIX B. Uncertainty Analysis

Table B.1 includes the sources of elemental error in the wind tunnel test for pressure coefficient uncertainty. These were identified by Shaw (1960), Erwin (1964), Arts et al. (1994), Mans et al. (2002), and Diaz (2006). In particular, the latter investigation was conducted on the same pressure measurement system that has been used to gather wind tunnel data at Western University. Additionally, the Cobra probe uncertainty for both velocities at reference height, $\overline{u}_{ref}$, and mean roof height, $\overline{u}_{z_{ref}}$, is 0.5 m/s (TFI website).

There are two types of error: bias and precision. The bias limit, B, refers to the systematic uncertainty that is unchanged between tests. On the other hand, the precision limit, S, refers to the random error that may be different between one test and the other. A summary of error sources for pressure and velocity measurements is shown in Table B.1.

Table B.1
Sources of measurement uncertainty for $C_{p,ref}$ and $C_{p,z_{ref}}$.

Error source	Reference	Value	Type
Scanner accuracy	Diaz (2006)	0.0305 [$C_{p,ref}$]	Bias
Scanner thermal zero shift	Diaz (2006)	0.0305 [$C_{p,ref}$]	Precision
Thermal Stability	Diaz (2006)	0.00061 [$C_{p,ref}$]	Precision
A/D Converter Accuracy	Diaz (2006)	0.0073 [$C_{p,ref}$]	Precision
A/D Converter Repeatability	Diaz (2006)	0.0073 [$C_{p,ref}$]	Precision
Terrain	Mans et al. (2002)	0.04 [$C_{p,ref}$]	Bias
Tap Dimension	Shaw (1960)	0.01 [$C_{p,ref}$]	Bias
Tap Burrs	Arts et al. (1994)	0.006 [$C_{p,ref}$]	Bias
Tap Angle	Erwin (1964)	0.001 [$C_{p,ref}$]	Bias
Cobra probe accuracy (for $C_{p,z_{ref}}$) ($w_{\overline{u}_{ref}}$, $w_{\overline{u}_{z_{ref}}}$)	TFI website	0.5 (m/s)	Bias

Considering all the elemental sources of bias and precision errors, the total bias (B_x) and precision uncertainty (S_x) for a variable, x, can be calculated by Eq. (B.1):

$$B_x = \left(\sum_{j=1}^{N_B} B_{j,i}^2\right)^{\frac{1}{2}} \; ; \; S_x = \left(\sum_{j=1}^{N_S} S_{j,i}^2\right)^{\frac{1}{2}}, \tag{B.1}$$

where N_B and N_S are the numbers of sources associated with bias and precision errors, respectively. The corresponding overall uncertainty, w_x, is computed by the combination of the bias and precision limits, as shown in Eq. (B.2):

$$w_x = \left[B_x^2 + (\check{t}S_x)^2\right]^{\frac{1}{2}}, \tag{B.2}$$

where the variable $\check{t}$ is the student t value. For the present study, a value of $\check{t} = 1.96$ is adopted, which corresponds to a 95 % confidence interval. Hence, one may estimate $w_{C_{p,ref}} = 0.0815$. To estimate the uncertainties associated with $C_{p,z_{ref}}$, one should combine $w_{C_{p,ref}}$ with the uncertainties of the wind velocity. A general quantity, R, function of multiple variables (e.g., x_1, x_2, …, x_N), may be written in mathematical terms as Eqn. (B.3):

$$R = f(x_1, x_2, \ldots, x_N). \tag{B.3}$$

The bounds of its uncertainty, w_R, may be described as $R \pm w_R$ (Wheeler & Ganji, A.R., 1996); assuming that the variables $x_1, x_2, \ldots, x_N$ are independent of one another, the combined uncertainty is estimated from the square roof of the sum of the squares of the individual component values (ASCE 49–21):

$$w_R = \left[\sum_{i=1}^{N} \left(w_{x_i} \frac{\partial R}{\partial x_i}\right)^2\right]^{\frac{1}{2}}. \tag{B.4}$$

Taking the definition of $C_{p,z_{ref,i}}$ into account (Eq. (9)), it results:

$$C_{p,z_{ref,i}} = f\left(C_{p,ref,i}, \overline{u}_{ref}, \overline{u}_{z_{ref}}\right). \tag{B.5}$$

Thus, applying Eq. (B.4) to Eq. (B.5):

$$w_{C_{p,z_{ref,i}}} = C_{p,z_{ref,i}} \left[\left(\frac{w_{C_{p,ref,i}}}{C_{p,ref,i}} \right)^2 + \left(2 \frac{w_{\overline{u}_{ref}}}{\overline{u}_{ref}} \right)^2 + \left(-2 \frac{w_{\overline{u}_{z_{ref}}}}{\overline{u}_{z_{ref}}} \right)^2 \right]^{\frac{1}{2}}. \tag{B.6}$$

To determine the uncertainty associated with the mean pressure coefficient $\overline{C}_{p,z_{ref,i}}$, $w_{\overline{C}_{p,z_{ref,i}}}$, and with the RMS pressure coefficient $\sigma_{Cp,z_{ref,i}}$, $w_{\sigma_{Cp,z_{ref,i}}}$, the standard error for the mean and RMS pressure coefficients are combined with $w_{C_{p,z_{ref,i}}}$:

$$w_{\overline{C}_{p,z_{ref,i}}} = \left[w^2_{C_{p,z_{ref,i}}} + \breve{t} Var\left[\overline{C}_{p,z_{ref,i}} \right] \right]^{\frac{1}{2}}, \tag{B.7}$$

$$w_{\sigma_{Cp,z_{ref,i}}} = \left[w^2_{C_{p,z_{ref}}} + \breve{t} Var\left[\sigma_{Cp,z_{ref,i}} \right] \right]^{\frac{1}{2}}, \tag{B.8}$$

where $Var\left[\overline{C}_{p,z_{ref,i}}\right]$ and $Var\left[\sigma_{Cp,z_{ref,i}}\right]$ are the standard error of the mean and RMS associated with the i-th pressure coefficient, determined by considering an independent sample set from the original time-history (Benedict and Gould, 1996). These new and shorter time-histories (constituted by a number of samples equal to N_{IS}) are determined by extracting from the original recording samples which are separated by an integral time scale defined as:

$$T_{IS} = \int_0^{t_i} R_{\overline{C}_{p,z_{ref,i}}} d\tau, \tag{B.9}$$

where $R_{\overline{C}_{p,z_{ref,i}}}$ is the autocorrelation function of $\overline{C}_{p,z_{ref,i}}$, and t_i is the first down-crossing of $R_{\overline{C}_{p,z_{ref,i}}}$ past 0. The new time-history, made up by means of the independent sample set, may be used the estimate $Var\left[\overline{C}_{p,z_{ref,i}}\right]$ and $Var\left[\sigma_{Cp,z_{ref,i}}\right]$ by recalling the expressions provided by Stuart and Ord (1994):

$$Var\left[\overline{C}_{p,z_{ref,i}}\right] = \left(\frac{m_2}{N_{IS}} \right)^{\frac{1}{2}}, \tag{B.10}$$

$$Var\left[\sigma_{C_{p,z_{ref,i}}}\right] = \left(\frac{1}{N_{IS}} \frac{m_4 - m_2^2}{4m_2} \right)^{\frac{1}{2}}, \tag{B.11}$$

where m_2 and m_4 are the second and fourth order statistical moments determined from the independent sample set.

Data availability

Data will be made available on request.

References

Acosta, T.J., Guo, Y., Wang, J., Brusco, S., Kopp, G.A., 2024a. Requirements for partial turbulence simulations using nondimensional turbulence energy contributions. J. Wind Eng. Ind. Aerod. 254, 105886. https://doi.org/10.1016/j.jweia.2024.105886.

Acosta, T.J., Brusco, S., Guo, Y., Wang, J., Kopp, G.A., 2024b. Consolidation of the ASCE 7 MWFRS Provisions: Part 2. Wind Tunnel Experiments on Buildings with 6:12 Roof Slopes. Faculty of Engineering, Western University, London, Canada.

Akon, A.F., Kopp, G.A., 2016. Mean pressure distributions and reattachment lengths for roof-separation bubbles on low-rise buildings. J. Wind Eng. Ind. Aerod. 155, 115–125. https://doi.org/10.1016/j.jweia.2016.05.008.

Akon, A.F., Kopp, G.A., 2018. Turbulence structure and similarity in the separated flow above a low building in the atmospheric boundary layer. J. Wind Eng. Ind. Aerod. 182, 87–100. https://doi.org/10.1016/j.jweia.2018.09.016.

Arts, T., Boerrigter, H., Carbonato, M., Charbonnier, J.M., 1994. Measurement Techniques in Fluid Dynamics. Von Karman Institute for Fluid Dynamics.

ASCE, 2021. Wind tunnel testing for buildings and other structures. ASCE49-21, American Society of Civil Engineers; Reston, VA, USA. https://doi.org/10.1061/9780784415740.

Asghari-Mooneghi, M., Irwin, P., Chowdhury, A., 2016. Partial turbulence simulation method for predicting peak wind loads on small structures and building appurtenances. J. Wind Eng. Ind. Aerod. 157, 47–62. https://doi.org/10.1016/j.jweia.2016.08.003.

Bearman, P.W., Morel, T., 1983. Effect of free stream turbulence on the flow around bluff bodies. Prog. Aero. Sci. 20 (2–3), 97–123. https://doi.org/10.1016/0376-0421(83)90002-7.

Benedict, L.H., Gould, R.D., 1996. Towards better uncertainty estimates for turbulence statistics. Exp. Fluid 22, 129–136.

Bruno, L., Salvetti, M.V., Ricciardelli, F., 2014. Benchmark on the aerodynamics of a rectangular 5:1 cylinder: an overview after the first four years of activity. J. Wind Eng. Ind. Aerod. 126, 87–106. https://doi.org/10.1016/j.jweia.2014.01.005.

Brusco, S., Acosta, T.J., Guo, Y., Wang, J., Kopp, G.A., 2024. Consolidation of the ASCE 7 MWFRS Provisions: Part 3. Data Comparison of Multiple Wind Tunnel Experiments. Faculty of Engineering, Western University, London, Canada.

Chen, X., Kwon, D.K., Kareem, A., 2014. High-frequency force balance technique for tall buildings: a critical review and some new insights. Wind Struct. 8 (4), 391–422. https://doi.org/10.12989/was.2014.18.4.391.

Cheng, C.M., Wang, J., 2004. Wind tunnel database for an intermediate wind resistance design of tall buildings. Proceedings of the 1st International Symposium on Wind Effects on Buildings and Urban Environment. Tokyo Polytechnic University, Tokyo, Japan.

Cook, N.J., Mayne, J.R., 1979. A novel working approach to the assessment of wind loads for equivalent static design. J. Wind Eng. Ind. Aerod. 4 (2), 149–164. https://doi.org/10.1016/0167-6105(79)90043-6.

CPP Inc, 2002. Data Report, Wind-Tunnel Tests – World Trade Center, New York, NY. Cermak, Peterka. Petersen Inc CPP Project 02-2420.

Davenport, A.G., King, J.P.C., 1984. Dynamic forces on long span bridges. 12th Congress of the International Association of Bridge and Structural Engineers. IABSE, Vancouver.

Diaz, P.S.Q., 2006. Uncertainty Analysis of Surface Pressure Measurements on Low-Rise Buildings. University of Western Ontario.

Erwin, J., 1964. Experimental techniques. In: Hawthorne, H. (Ed.), Aerodynamics of Turbines and Compressors, pp. 167–269. New Jersey.

Estephan, J., Chowdhury, A.G., Irwin, P., 2022. A new experimental-numerical approach to estimate peak wind loads on roof-mounted photovoltaic systems by incorporating inflow turbulence and dynamic effects. Eng. Struct. 252, 113739. https://doi.org/10.1016/j.engstruct.2021.113739.

Fritz, W.P., Bienkiewicz, B., Cui, B., Flamand, O., Ho, T.C.E., Kikitsu, H., Letchford, C.W., Simiu, E., 2008. International comparison of wind tunnel estimates of wind effects on low-rise buildings: test-related uncertainties. J. Struct. Eng. 134, 1887–1890. https://doi.org/10.1061/(ASCE)0733-9445(2008)134:12(1887).

Gavanski, E., Gurley, K.R., Kopp, G.A., 2016. Uncertainties in the estimation of local peak pressures on low-rise buildings by using the Gumbel distribution fitting approach. J. Struct. Eng. 142 (11), 04016106. https://doi.org/10.1061/(ASCE)ST.1943-541X.0001556.

Guo, Y., Wu, C.-H., Kopp, G.A., 2021. A method to estimate peak pressures on low-rise building models based on quasi-steady theory and partial turbulence analysis. J. Wind Eng. Ind. Aerod. 218, 104785. https://doi.org/10.1016/j.jweia.2021.104785.

Guo, Y., Wang, J., Acosta, T.J., Brusco, S., Kopp, G.A., 2025. Methodology for obtaining aerodynamic coefficients for unified wind loading provisions. J. Struct. Eng. 151 (11), 04025182. https://doi.org/10.1061/JSENDH/STENG-14983.

Ha, Y.C., Kim, D.W., Kil, Y.S., 2004. Characteristics of the across-wind fluctuating force and spectral density of rectangular high-rise buildings with various side ratios. Proceedings of the CTBUH 2004. CTBUH, Seoul, Korea.

Ho, T.E., Surry, D., Morrish, D., Kopp, G.A., 2005. The UWO contribution to the NIST aerodynamic database for wind loads on low buildings: Part 1. Archiving format and basic aerodynamic data. J. Wind Eng. Ind. Aerod. 93 (1), 1–30. https://doi.org/10.1016/j.jweia.2004.07.006.

Holmes, J.D., Tse, T.K., 2014. International high-frequency base balance benchmark study. Wind Struct. 18 (4), 457–471. https://doi.org/10.12989/was.2014.18.4.457.

Hong, H.P., Li, S.H., Mara, T.G., 2013. Performance of the generalized least-squares method for the Gumbel distribution and its application to annual maximum wind speeds. J. Wind Eng. Ind. Aerod. 119 (7), 121–132. https://doi.org/10.1016/j.jweia.2013.05.012.

Irwin, P., 1979. Correction of distortion effects caused by tubing systems in measurements of fluctuating pressures. J. Wind Eng. Ind. Aerod. 5 (1–2), 93–107. https://doi.org/10.1016/0167-6105(79)90026-6.

Irwin, P.A., 1998. The role of wind tunnel modelling in the prediction of wind effects on bridges. In: Proceedings of the International Symposium Advances in Bridge Aerodynamics, 10–13 May, Copenhagen. Balkema, Rotterdam, pp. 99–117.

Irwin, P., 2003. Personal Communication Letter from Dr. Peter Irwin to Dr. Emil Simiu, Dated Nov. 7, 2003 Re: World Trade Center Wind Tunnel Investigations CPP/RWDI Data Comparison. RWDI Reference #02-1310.

Irwin, P.A., 2008. Bluff body aerodynamics in wind engineering. J. Wind Eng. Ind. Aerod. 96 (6–7), 701–712. https://doi.org/10.1016/j.jweia.2007.06.008.

Kopp, G.A., 2023. Updates to the wind tunnel method for determining design loads in ASCE 49-21. Wind Struct. 37, 163–178. https://doi.org/10.12989/was.2023.37.2.163.

Kopp, G.A., Wang, J., Guo, Y., Brusco, S., Acosta, T.J., 2024. Consolidation of the ASCE 7 MWFRS Provisions: Part 4. Differences between Current Proposal and the Original Data Sources for Chapters 27 & 28. Faculty of Engineering, Western University, London, Canada.

Kopp, G.A., Wang, J., Guo, Y., Brusco, S., Acosta, T.J., 2025. Assessment of the main wind force resisting system provisions of ASCE/SEI 7-22 for rigid buildings. J. Struct. Eng. https://doi.org/10.1061/JSENDH/STENG-14984 in press.

Kwan, K., Kopp, G.A., 2021. The effects of edge radius on wind tunnel tests of low-rise buildings. J. Wind Eng. Ind. Aerod. 214, 104668. https://doi.org/10.1016/j.jweia.2021.104668.

Levy, M., Abboud, N., 2004. World Trade Center Structural Engineering Investia Levy, M. And Abboud, N., Oct. 4, 2002, Structural Engineering Investigation of the World Trade Center, Expert Report, Hart-Weidlinger. Weidlinger Associates, Inc.. (Accessed 1 August 2002)

Lieblein, J., 1974. Efficient Methods of Extreme-Value Methodology. Rep. No. NBSIR 74-602. National Bureau of Standards, Washington, DC.

Lin, N., Letchford, C., Tamura, Y., Liang, B., Nakamura, O., 2005. Characteristics of wind forces acting on tall buildings. J. Wind Eng. Ind. Aerod. 93 (3), 217–242. https://doi.org/10.1016/j.jweia.2004.12.001.

Liu, Y., Kopp, G.A., Chen, S.-F., 2019. Effects of plan dimensions on gust wind loads for high-rise buildings. J. Wind. Eng. Ind. Aerod. 194, 103980. https://doi.org/10.1016/j.jweia.2019.103980.

Lunghi, G., Pasqualetto, E., Rocchio, B., Mariotti, A., Salvetti, M.V., 2022. Impact of the lateral mean recirculation characteristics on the near-wake and bulk quantities of the BARC configuration. Wind Struct. 34 (1), 115–125. https://doi.org/10.12989/was.2022.34.1.115.

Lunghi, G., Brusco, S., Mariotti, A., Piccardo, G., Salvetti, M.V., 2024. Influence of inflow acceleration on the aerodynamic characteristics of a square cylinder. J. Wind Eng. Ind. Aerod. 252, 105814. https://doi.org/10.1016/j.jweia.2024.105814.

Mannini, C., Marra, A.M., Pigolotti, L., Bartoli, G., 2017. The effects of free-stream turbulence and angle of attack on the aerodynamics of a cylinder with rectangular 5:1 cross section. J. Wind Eng. Ind. Aerod. 161, 42–58. https://doi.org/10.1016/j.jweia.2016.12.001.

Mans, C., Ho, T.C.E., Surry, D., Kopp, G.A., 2002. The Factory Mutual Sensitivity Study. University of Western Ontario.

Mariotti, A., Lunghi, G., Salvetti, M.V., 2024. Experimental investigations on the effect of upstream-edge rounding on the BARC configuration. J. Wind Eng. Ind. Aerod. 251, 105787. https://doi.org/10.1016/j.jweia.2024.105787.

Melbourne, W.H., 1980. Comparisons of measurements on the CAARC Standard tall building model in simulated model wind flows. J. Wind Eng. Ind. Aerod. 6 (1–2), 73–88. https://doi.org/10.1016/0167-6105(80)90023-9.

Mokhtar, N.O., Fernández-Cabán, P.L., Catarelli, R.A., 2025. Investigating low-frequency turbulence effects on building roof pressures through active flow control in a large boundary layer wind tunnel. J. Wind Eng. Ind. Aerod. 258, 106009. https://doi.org/10.1016/j.jweia.2025.106009.

Morrison, M.J., Kopp, G.A., 2018. Effects of turbulence intensity and scale on surface pressure fluctuations on the roof of a low-rise building in the atmospheric boundary layer. J. Wind Eng. Ind. Aerod. 183, 140–151. https://doi.org/10.1016/j.jweia.2018.10.017.

NIST, 2009. Toward a standard on the wind tunnel method. NIST Technical Note 1655.

Obasaju, E.D., 1992. Measurement of forces and base overturning moments on the CAARC tall building model in a simulated atmospheric boundary layer. J. Wind Eng. 40, 103–126. https://doi.org/10.1016/0167-6105(92)90361-D.

Roshko, A., 1993. Perspectives on bluff-body aerodynamics. J. Wind Eng. Ind. Aerod. 49, 79–100. https://doi.org/10.1016/0167-6105(93)90007-B.

RWDI, 2002a. Wind Induced Structural Responses, World Trade Center – Tower 1, New York, New York. Prepared for Hart-Weidlinger Division of Weidlinger Associates. Inc. Rowan Williams Davies & Irwin, Inc., Guelph, Ontario, Canada.

RWDI, 2002b. Wind Induced Structural Responses, World Trade Center – Tower 2, New York, New York. Prepared for Hart-Weidlinger Division of Weidlinger Associates. Inc. Rowan Williams Davies & Irwin, Inc., Guelph, Ontario, Canada.

Saathoff, P.J., Melbourne, W.H., 1997. Effects of free-stream turbulence on surface pressure fluctuations in a separation bubble. J. Fluid Mech. 337, 1–24. https://doi.org/10.1017/S0022112096004594.

Shaw, R., 1960. Influence of hole dimension on static pressure measurements. J. Fluid Mech. 7 (2), 550–564.

Shelley, E., Hubbard, E., Zhang, W., 2023. Comparison and uncertainty quantification of roof pressure measurements using the NIST and TPU aerodynamic databases. J. Wind Eng. Ind. Aerod. 232, 105246. https://doi.org/10.1016/j.jweia.2022.105246.

Stathopoulos, T., Surry, D., 1983. Scale effects in wind tunnel testing of low buildings. J. Wind Eng. Ind. Aerod. 13, 313–326. https://doi.org/10.1016/0167-6105(83)90152-6.

Stuart, A., Ord, J.K., 1994. Kendall's Advanced Theory of Statistics, sixth ed. John Wiley & Sons, New York.

Tanaka, H., Lawen, N., 1986. Test on the CAARC standard tall building model with a length scale of 1 : 1000. J. Wind Eng. Ind. Aerod. 25 (1), 15–29. https://doi.org/10.1016/0167-6105(86)90102-9.

TFI website: https://www.turbulentflow.com.au/Products/CobraProbe/CobraProbe.php.

Vickery, P.J., Surry, D., Isyumov, N., 2003. Report Regarding the Review of the World Trade Center Twin Towers (NY) Wind Studies Carried Out by RWDI and CPP. The Alan G. Davenport Wind Engineering Group and the Boundary Layer Wind Tunnel Laboratory at the University of Western Ontario, London, Ontario, Canada.

Wang, J., Kopp, G.A., 2021. Comparisons of aerodynamic data with the main wind force–resisting system provisions of ASCE 7-16. II: mid-and high-rise buildings. J. Struct. Eng. 147 (3), 04020348. https://doi.org/10.1061/(ASCE)ST.1943-541X.0002925.

Wheeler, A.J., Ganji, A.R., 1996. Introduction to Engineering Experimentation, first ed. Prentice Hall, New Jersey.

Yu, D., Butler, K., Kareem, A., Glimm, J., Sun, J., 2013. Simulation of the influence of aspect ratio on the aerodynamics of rectangular prisms. J. Eng. Mech. 139 (4), 429–438. https://doi.org/10.1061/(ASCE)EM.1943-7889.0000494.

Zhu, Y., Zhou, X., Chen, Y., Ma, C., Wang, L., Zheng, C., Yan, B., 2025. Comparison of aerodynamic effects on the Commonwealth advisory aeronautical research Council (CAARC) tall building model tested in two wind tunnel laboratories. Appl. Sci. 15, 811. https://doi.org/10.3390/app15020811, 2025.